

Unlocking the Ion Migration in Solid-State Electrolytes via Path Entropy

Qiye Guan^{a,*}, Kaiyang Wang^b, Jingjie Yeo^b, and Yongqing Cai^{a,*}

^aInstitute of Applied Physics and Materials Engineering, University of Macau, Taipa, Macau, China

^bDepartment of Materials Science and Engineering, Cornell University, Ithaca, New York 14853, United States

*Corresponding authors: yc07819@connect.um.edu.mo, yongqingcai@um.edu.mo

Abstract

Promoting ionic diffusion by reducing activation energy, as a thermally activated process following the Arrhenius relation, is a fundamental principle in designing materials for electrochemical batteries. However, this scenario is constrained by the enthalpy-entropy compensation mechanism (Meyer-Neldel Rule, MNR), which is ubiquitously observed in biological process and chemical reactions. This sets a limitation of promoting ion transport by reducing activation enthalpy. Notably, certain solid-state electrolytes characterized by disordering or degenerate saddle states exhibit anomalous behaviours and disobey MNR, suggesting the existence of an elusive source of entropy. Herein we propose the concept of path entropy (S_p) governs kinetic process in dense and mobile ionic systems such as lithium diffusion in solid-state electrolytes. By integrating Markov state method, well-tempered metadynamics, and machine learning-based softness analysis, we elucidate the intricate relationship between fast ionic hopping and microscopic local environments in inorganic thiophosphates. The S_p accounts for a strong fluctuation of free energy landscape perceived by Li cations and enables an assessment of their collective diffusion behaviour as well. A unified framework is established for handling time-evolved and group-collective ionic kinetics, which exploits pathway frustration, transcending common “static” scenario in traditional entropy-driven approach based on compositional multiplicity. This provides a new dimension for connecting structural disorder and the freedom of ionic diffusion pathways, suitable for a wide range of ionic-driven applications such as battery, superionic conductors and neuromorphic devices.

Main

Recent years have underscored the importance of batteries for storing intermittent renewable energy¹. In particular, ionic conduction in redox batteries has gained prominence, rivalling electronic conduction's transformative impact on society². While both types of conduction rely on specific host materials, ions exert more profound effects on accommodating materials³. In pursuit of all-solid-state metal batteries with enhanced energy density and safety, solid-state electrolyte (SSE) materials with high ionic conductivity has gained significant attention^{4,5}. Embedded with intrinsically dense conducting ions, SSE possesses intrinsically more complex ionic kinetics involving many-body and group concerted motion than normal defect kinetics of single entity and classical ionic conductors⁵. Conduction induced bond breaking/reorganization in SSE lattices is frequent (up to 40 THz⁶), implying strong and instantaneous fluctuations of enthalpy and entropy (**Fig. 1**). The study of ionic conduction in SSE is not merely of technical interest; it also reignites interests in some perplexing issues that have persisted for decades from the scientific side.

The traditional understanding of ionic conduction relies on the Arrhenius law, where rate observable X follows an exponential relationship with temperature: $X = X_0 e^{-\Delta E/k_B T}$, where X_0 is the pre-factor, ΔE is the activation energy, T is the temperature, and k_B is the Boltzmann constant. Promotion of X is usually assumed to be achieved by reducing the ΔE . However, experiments have frequently observed the rate variable such as ionic conductivity (σ) decreases as the ΔE decreases and vice versa^{7,8}. These findings challenge the paradigm that lowering ΔE always leads to a higher σ . In fact, a more rigorous form involves the free energy $\Delta G = \Delta H - T\Delta S$, where the effort of lowering activation enthalpy (ΔH) can be counteracted by an increase in entropy (ΔS) through the pre-factor term $X_0 \propto e^{\Delta S/k_B}$. This effect governs the Meyer-Neldel Rule (MNR)⁹, also known as the isokinetic law¹⁰ or the entropy-enthalpy compensation law¹¹, which sparks intense examinations as early as the 1930s. Considering that configurational entropy (S_c) fluctuates weakly, the compensating entropy is suspected to function in the form of diffusion vacancies¹², and multi-excitation entropy for activated process with a large barrier¹³. Notably, while the MNR has been extensively observed in the domains of chemical and biological kinetics¹⁴, its application requires caution when the activation enthalpy is

comparable to thermal excitation¹⁵. The MNR fails in systems, for instance, with frustrated lattice frameworks such as $\text{LiTi}_2(\text{PS}_4)_3$, a type of SSE where disordered pathways suppress compensation and induce superionic diffusion through a frustrated energy landscape^{16,17}. For Ag/Na/K-substituted β -alumina SSE, their pre-factors increase more rapidly at lower activation energy values than at high values¹⁸. All these infer the existence of somehow hidden source of entropy, which has garnered considerable scrutiny^{13,15,19}. So far, most efforts assumed an overall static configuration⁵, either based on a thermostatic scenario or within the transition state theory²⁰. Unfortunately, the approaches with neglecting correlation of particles cannot explain the experimentally observed changes in the pre-factor for $\text{Li}_6\text{PS}_5\text{X}$ and $\text{Na}_3\text{PS}_{4-x}\text{Se}_x$.^{7,8} A fundamental question remains: What drives the entropy of activation in dense ionic conductors marked by cooperative behavior and complex dynamics?

Herein, we present a paradigm to articulate the entropy by linking the concept of ion diffusion with path entropy (S_p), a measure that quantifies the multiplicity of pathways traversed by lithium ions, as inspired from principles of information theory²¹. Akin to the approach of Miller–Abrahams approximation²², the pioneering work of electron conduction in semiconductor, site transfer of dense mobile ions is explicitly included by transition path theory. Our integrated framework, which combines configurational and path entropies, is essential for elucidating the intricate relationships between structural modifications and ion diffusion (**Fig. 1**). Using Li-argyrodites SSE as a case study, through large-scale machine-learned molecular dynamics simulations, we demonstrate that the magnitude of the S_p can approach the level of enthalpy barriers, signifying the prospect of entropic driven design of electrolyte instead of traditional enthalpy scenario. This integrated approach is also used to examine and validate the concept of lithium softness^{23,24}, a measure of collective ion diffusion and a framework for analysing temporal phenomena of ionic conduction, which is desired for approaching the history/memory effect in a wealth of ionic-driven applications like neuromorphic devices, batteries, and resistive switching.

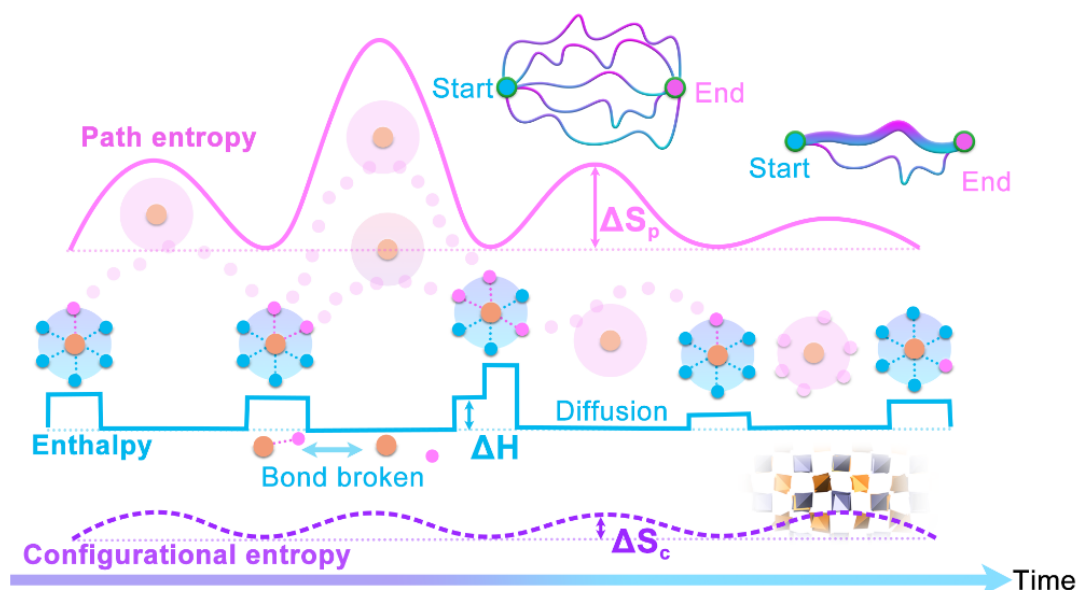


Fig. 1. Schematic illustration of the temporal evolution of thermodynamic variables associated with Li diffusion in SSE. The ΔS_p , ΔS_c , and ΔH are the changes in path entropy, configurational entropy, and enthalpy, respectively.

Results and discussion

Among various SSE families, including halides, oxides, and polymers, sulfides are particularly notable for their high σ (10^{-5} to 10^{-2} S/cm)²⁵. Li-argyrodites ($\text{Li}_{7-x}\text{BC}_{6-x}\text{D}_x$, $0 < x < 1$, B = P or As; C = S or Se; D = Cl, Br or I), a prominent subtype within the sulfide family, are distinguished by their facile synthesis process and high σ ²⁶, with rich polyanionic moieties²⁷. Here we examine the P-S-Cl based argyrodites, $\text{Li}_6\text{PS}_5\text{Cl}$ with its two polymorphs with $Amm2$ and $F\bar{4}3m$ space groups, denoted as LPSCI-I and LPSCI-II, respectively (**Fig. 2a and b**). Both phases entail a phosphorus-sulfur framework, in the form of rigid $[\text{PS}_4]^{3-}$ tetrahedra (**Fig. 2c**), which acts as the backbone for accommodating lithium ions arranged in flexible coordination shells.

Based on LPSCI-II, we introduce Li vacancies and site disorder (sulfur and chloride in Wyckoff sites 4a and 4c) to form LPSCI-III phase with a composition of $\text{Li}_{5.5}\text{PS}_{4.5}\text{Cl}_{1.5}$. Its atomic structure (**Fig. 2d**) is obtained using the cluster expansion method, with reference to experimental results²⁸ (**Supplementary Figures 1-3**). In addition, to regulate the interaction between the anion framework and the flexible

lithium coordination shell, another variant named LSPSCI was constructed by replacing P with Si in the rigid $[\text{PS}_4]^{3-}$ unit of LPSCI-II, with the formula of $\text{Li}_{20}\text{Si}_3\text{P}_3\text{S}_{23}\text{Cl}$ (**Fig. 2e**).

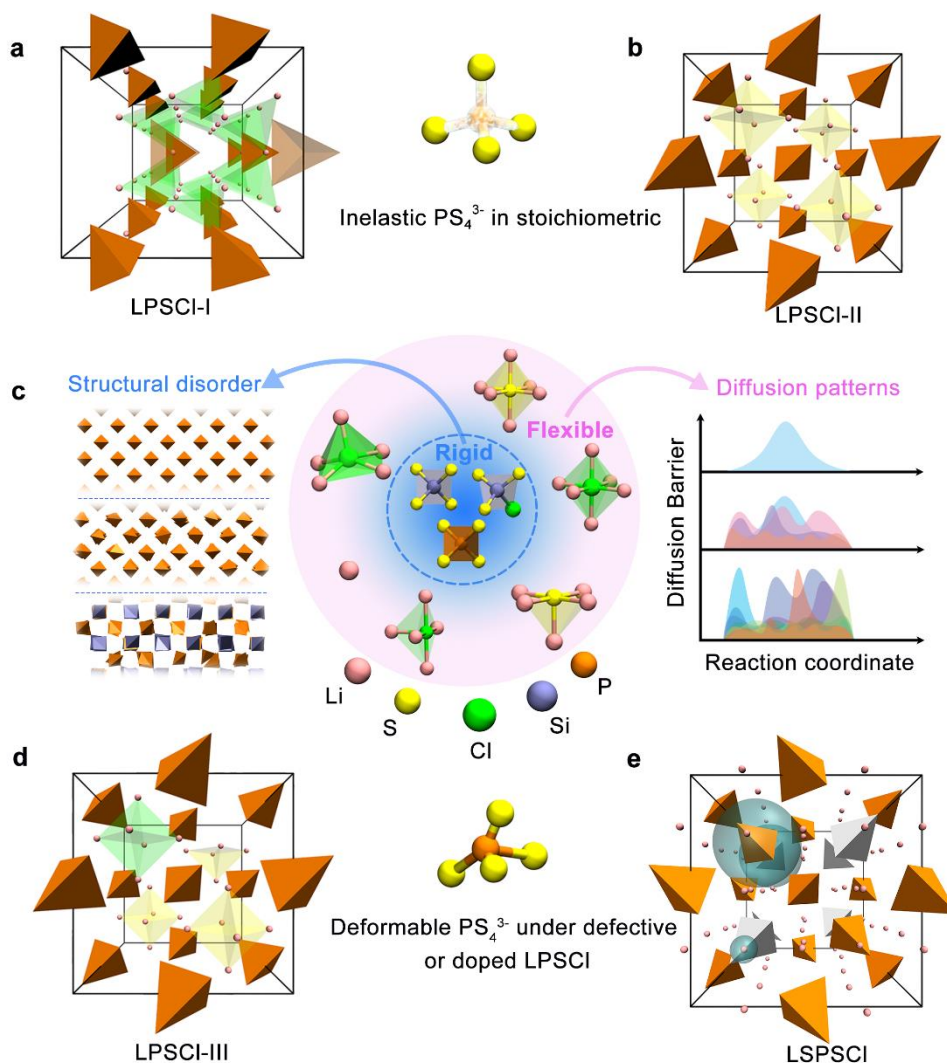


Fig. 2. Structural variants of argyrodite-type SSEs, composed of two types of shells: soft “lithium shells” centered by S or Cl, and rigid tetragons of “sulfur shells” centered by P or doped Si. **a-b**, Crystal structures of $\text{Li}_6\text{PS}_5\text{Cl}$ LPSCI-I and LPSCI-II polymorphs with $Amm2$ and $F\bar{4}3m$ space groups, respectively. **c**, Illustration of disordering associated with flexible lithium coordination shells and reoriented rigid $[\text{PS}_4]/[\text{SiS}_4]$ units. **d**, Crystal structure of LPSCI-III ($\text{Li}_{5.5}\text{PS}_{4.5}\text{Cl}_{1.5}$) with addition of Li vacancies and site disorder based on LPSCI-II. **e**, Crystal structure of LSPSCI ($\text{Li}_{20}\text{Si}_3\text{P}_3\text{S}_{23}\text{Cl}$) through replacing P with Si in the rigid $[\text{PS}_4]^{3-}$ unit of LPSCI-II. In LPSCI-I, -II, and -III models, the flexible lithium shells centered with S and Cl are colored in yellow and green color, respectively. While in LSPSCI lithium

shells are colored light blue. In all phases, the P-centered and Si-centered sulfur shells are shown by solid orange and silver tetrahedrons, respectively.

Here, diverging from conventional “single-ion” methods, such as the nudged elastic band, which are suitable for analysing activation involving single or few entities, we address the kinetic behaviours of a multitude of lithium ions, reflecting the situation in batteries, by designing lattice-based Markov state models (MSMs) and using well-tempered metadynamics (WTmetaD). Lithium diffusion is mediated by occupying/emptying discrete sublattice sites in SSEs, forming a continuous-time Markov chain in a discrete state space. To ensure a proper lag time to allow sufficient transitions among the discrete states, as usually the main challenge in modeling the Markov chain²⁹, we employ ab initio molecular dynamics (AIMD) and neural-network potentials (NNPs) trained with comparable accuracy of density functional theory (DFT), to conduct large-scale simulations spanning nanometer-length and nanosecond-time scales on complex systems of thousands of atoms. (**Supplementary Tables 1-2, Supplementary Figures 4-9**).

The lithium ions are self-organized to form lithium coordination shells (LCSs) in forms of polyhedrons (**Fig. 3a-3d** and **Supplementary Figure 10**) where the vertices are sites for Li occupation. The LCSs for LPSCI-I, LPSCI-II, LPSCI-III, and LSPSCI are characterized, respectively, by a Cl-centered square pyramid coordinated with five Li (**Supplementary Figure 11**), a S-centered octahedron (**Fig. 3a**), a S or Cl centered octahedron coordinated with six Li atoms (**Fig. 3b, 3c**), and a reconstructed shell coordination with twelve Li atoms (**Fig. 3d, 3e**).

We discretize the local space surrounding the central anionic atoms (i.e. S or Cl) in these LCSs (**Fig. 3a-e**) to construct the Markov model, generating 5 states reflecting Li occupancy in LPSCI-I, 7 states for LPSCI-II and LPSCI-III, and 13 states for LSPSCI. The LCSs are flexible and Li hopping among the vertex is equivalent to dynamic sampling of the vertex space. A hop between vertex sites means a state transfer. Therefore, each type of the LCS forms a characteristic manifold with unique Li spatial and angular distribution. By resorting to the Markovian approach, time-evolving states hence encode the multiplicity of hopping pathways among the discrete sites. The detailed workflow is summarized in **Supplementary Figure 12**, through which a spatial mapping of the Li trajectories into these LCSs is possible. Notably, the

square pyramid-type LCSs in LPSCI-I disfavours cross-site intra-cage motion of Li, inducing a nearly frozen discrete space and impaired dynamics (**Supplementary Figure 13**), while significant intra-cage state transfer is observed within octahedron-type LCSs in LPSCI-II (**Fig. 3f**), even more prominent compared to Li deficient LPSCI-III (**Fig. 3g** and **Supplementary Figure 14**). Nevertheless, the macroscopic ion conduction is limited by abilities of long-range migration instead of short-range ion transfer.³⁰ Li-vacancy-contained LPSCI-III has more frequent inter-cage coupling and a higher σ compared to LPSCI-II. In the case of LSPSCI, substituting P with Si expands the state space of lithium ions and, meanwhile, promotes inter-cage diffusion among LCSs compared to pristine LCS. (**Supplementary Figure 15**)

A typical discrete Markov-chain process entails three parts: a discrete state space, a transition matrix defining the probabilities of transition from one state to another, and an initial distribution across the state space. Here the state space of Li conduction in SSEs is constructed by discretizing the LCSs. In other words, the ideal Li positions in pristine LCS (**Fig. 3h** and **3i**) constitute a local surrounding shell space which can be discretized in the form of set $\{X_i\}_{i=1}^n$, where each X_i represents the i th isolated segment state basis capable of accommodating one Li ion (LS_i in **Fig. 3f** and **3g**, i is an integer), and n is the total number of discrete lithium states (LS). This discretization enables reconstruction of the lithium-ion hopping dynamics as a Markov process (referring details in methods), which we illustrate with an example in **Fig. 3j**. Specifically, the slowest three lithium diffusion dynamic processes in the discrete space of LPSCI-II are resolved.

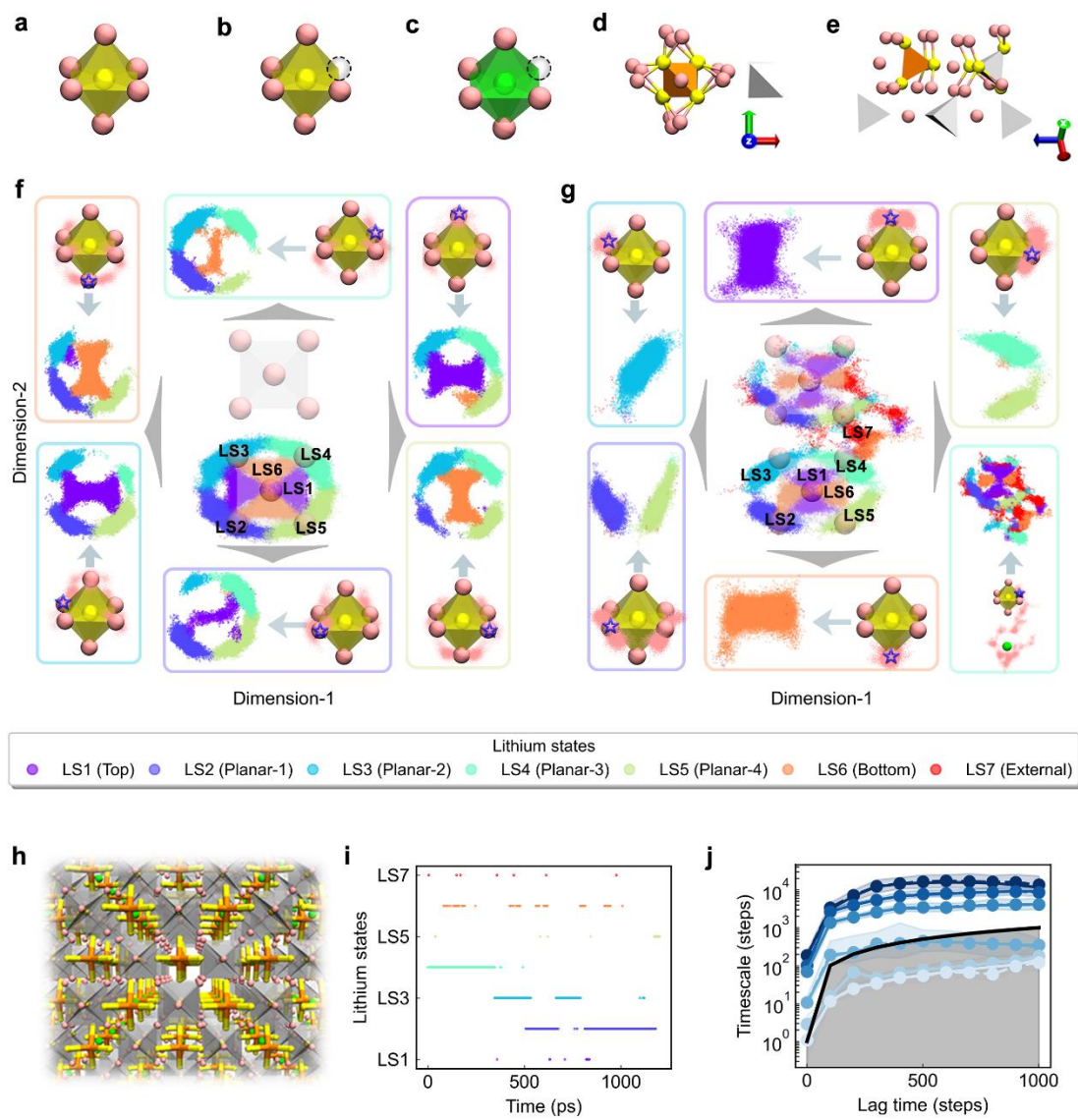


Fig. 3. Construction of the Markov state of lithium. Lithium coordination shells (LCSs) in **a**, LPSCI-II/LPSCI-III, **b**, LPSCI-III (S centered), **c**, LPSCI-III (Cl centered), **d**, LPSCI (top view), and **e**, LPSCI (front view). Note vacancies are represented with dashed circles. The Li, P, S, and Cl atoms are colored pink, orange, yellow, and green, respectively. **f-g**, Projected discrete lithium trajectories from 3D space in one LCS of LPSCI-II (**f**) and LPSCI-III (**g**). The center panel (edge panels) represents trajectories of all (isolated) Li atoms in this LCS to its adjacent LCS. Various lithium docking states (LS_{*i*}, *i*=1, 2, 3, ...) are classified with different colors. The initial position of the selected lithium atom analysed is denoted with star and the trajectories in 3D space are coloured pink. The arrow indicates a projection of the lithium trajectory of one specific lithium atom into various LS_{*i*} states in LCS. **h**, 3D

visualization of the LCSs in pristine LPSCI-II. **i**, Time evolving state of one lithium atom up to one nanosecond with the time resolution of 20 fs varying over LS_i states in LCS for the LPSCI-II. **j**, Implied time scale plot of Markov process in LPSCI-II. The lines beneath the black line correspond to processes that are faster than the lag time.

Mapping Li trajectories into the discrete space allows one to obtain the mean first passage time (MFPT)³¹, reflecting the average time (in steps) it takes to reach one X_i state when starting from another X_j state. The MFPT analysis of LPSCI-II and LPSCI-III, as illustrated in **Fig. 4a** and **4b**, respectively, reveals distinct time variation for inter-cage site hopping. As shown in the 7th column (LS7) in **Fig. 4a** and **4b**, corresponding to states transfer from LS_i ($i=1-6$) \rightarrow LS7, lithium atoms take only about 70 ps to leave the original LCS for its neighboring LCS in LPSCI-III, while such inter-cage hopping is more sluggish in LPSCI-II. This difference suggests that the lithium vacancies and S/Cl site disorder in LPSCI-III strongly accelerate the inter-cage hopping. However, compared to the short time (20 to 40 ps) needed for site hopping within the LCS of LPSCI-II, LPSCI-III shows suppressed intra-cage hopping with its MFPT ranging from 60 ps to 120 ps. In Si-doped case of LSPSCI, the lithium diffusion kinetics vary substantially, ranging from nearly instantaneous to completely forbidden migration (**Supplementary Figure 16**). While certain sites (such as LS11 and LS12) are blocked under room temperature, the formation of various meta-states, twice as many as the original LCS from LPSCI-II, facilitates the lithium diffusion across multiple locations. Like LPSCI-III, inter-cage hopping (other lithium sites \rightarrow LS13) is fast with very short passage times, averaging only a few picoseconds. As expected, increasing the temperature promotes lithium jumping kinetics for all the phases. (**Supplementary Figures 17, 18, and 19**)

We next delve into the mechanisms underlying states transfer in discrete space through transition path theory (TPT). Both LPSCI-III and LSPSCI exhibit diverse flow patterns compared to the pristine LPSCI-II. Li pathways in LPSCI-II are simple, reflected by four the transition between the apical top state (LS1) to the four equatorial planar states (LS2 to LS5) in **Fig. 4c** and **Supplementary Figure 20**, contrasting with complex pathways in LPSCI-III (**Figure 4d, Supplementary Figure 21**) which largely stem from transitions across LCSs. Through TPT, the versatile

lithium diffusivity among the polymorphs can be quantitatively assessed via introducing path entropy S_p of lithium defined by a Shannon entropy²¹-like term as

$$S_p = - \sum_{i \neq j} f'_{ij} \ln f'_{ij} \quad (1)$$

where f' represents a normalized form of transition flow matrix f , (detailed definitions of f and its component f_{ij} is referred to the methods section), with its components f'_{ij} corresponding to magnitude of net lithium flux covering all the possible diffusion paths between different states i and j . As depicted in **Fig. 4e** and **Supplementary Table 3**, LPSCI-III has a higher S_p than LPSCI-II for almost all lithium flux paths, indicating unlocked migration paths that facilitate easier diffusion throughout the LCSs. Furthermore, reconstruction of the LCS via chemical doping of the anion framework as in LSPSCI introduces various intermediate states which induce diverse flow patterns and significantly increased S_p . Compared to the intrinsic LPSCI-II phase, the number of potential diffusion pathways between one specific site to any other sites are extensive, involving up to 11 intermediate sites. By selecting LS1 as the starting point of diffusion, many pathways are activated and have high S_p , despite some diffusion paths being blocked (e.g. LS1→LS2, LS1→LS11, and LS1→LS12) (**Fig. 4f**, **Supplementary Table 4**, and **Supplementary Figure 22**), indicating a strong effect of chemical modification of the anionic framework on modifying microscopic Li diffusion routes. Notably, the inter-cage hopping (LS1→LS13) in LSPSCI exhibits the highest S_p of 2.99 (**Fig. 4e**), signifying significantly strengthened flexibility of the LCS regulated by Si substitution.

From an alternative perspective to S_p , a free energy analysis is conducted to evaluate the feasibility and spontaneity of diffusion processes. Using WTmetaD simulation, we investigate lithium diffusion across LCSs, distinguishing between intra and inter-cage diffusion. By defining collective variables (CVs) as distances to the centers of LCSs, (**Supplementary Note 2.1**, **Supplementary Figures 23**) we confirm a moderate diffusion barrier (~ 38 kJ/mol) of inter-cage motion across neighboring LCSs in LPSCI-III compared to LPSCI-II (~ 65 kJ/mol, **Fig. 4g**, **4h**, and **Supplementary Figures 24** and **25**), implying accelerated kinetics for inter-cage diffusion in LPSCI-III. In contrast, in accordance with S_p , intra-cage motion is more

sluggish in LPSCI-III than LPSCI-II (**Supplementary Note 2.2, Figures 4i, 4j, Supplementary Figures 26 and 27**), which is indicative of the higher barrier of the former. In LPSCI-II, lithium atoms adopt a barrier of approximately 13.4 kJ/mol for intra-cage diffusion, while in Li-vacant LPSCI-III, the barrier for intra-cage diffusion in sulfur-centered LCSs (S-LCSs) is 34.1 kJ/mol and 14.5 kJ/mol for chlorine-centered LCS (Cl-LCSs). This discrepancy between LPSCI-II and LPSCI-III may stem from the greater freedom within the softer LCS of LPSCI-III, prompting lithium atoms to prefer inter-cage hopping over intra-cage site hopping. We also explore a concerted migration of lithium in argyrodite-type SSEs, a type of migration involving simultaneous diffusion of two lithium ions, as proven to exist in LLZO³². By using WTmetaD simulations with designed CVs in LPSCI-II (**Fig. 4k, Supplementary Notes 2.3, Supplementary Figures 29 and 30**), concerted migration of two lithium ions from neighbouring LCSs along the predefined path s exhibits a free energy barrier lower than 35 kJ/mol, significantly lower than inter-cage diffusion involving a single lithium atom.

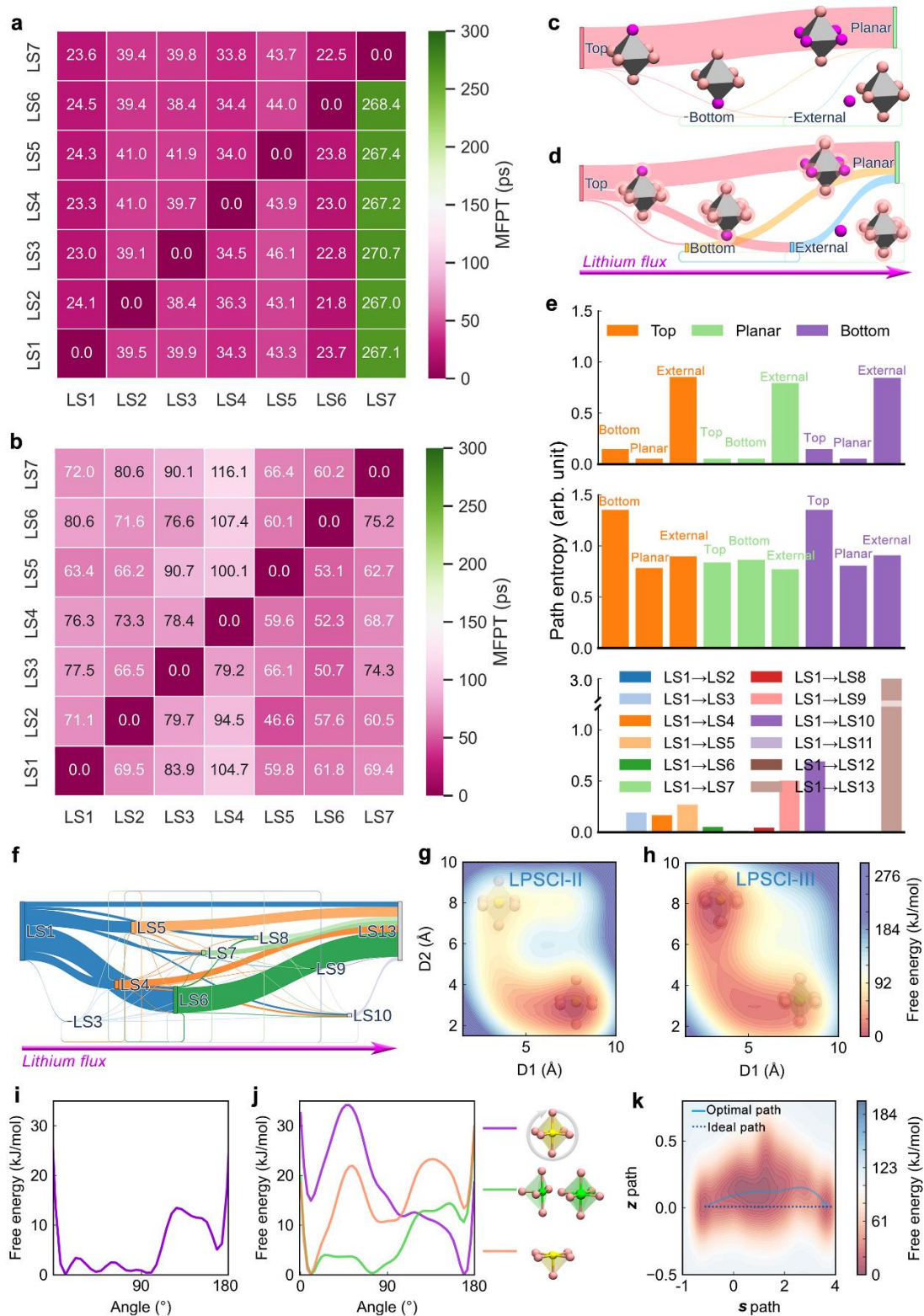


Fig. 4. Kinetics and thermodynamics analysis of lithium diffusion. **a-b**, The MFPT heatmap of LPSCI-II and LPSCI-III at room temperature, respectively. **c-d**, Decomposed pathways for the lithium flux in LCSs of LPSCI-II (**c**) and LPSCI-III (**d**) from initial site (top apical site, LS1) to end site (any planar equatorial sites, LS2-LS5)

in an octahedron, via direct and “bottom” apical site intra-cage motions or “external” sites with an inter-cage motion. **e**, Path resolved contribution of S_p for Li diffusion in LPSCI-II (top panel), LPSCI-III (middle panel), LSPSCI (bottom panel). For LPSCI-II and LPSCI-III, the colors (orange, green, and purple) of the bars indicate the initial states (top, bottom, and planar) of the lithium. **f**, The lithium diffusion flux from LS1 to LS13 in LCSs of LSPSCI. **g-h**, Free energy plot of inter-cage lithium diffusion of LPSCI-II and LPSCI-III. D1 and D2 are distances between lithium ion to centers of two adjacent LCS, respectively. **i-j**, Free energy plot of intra-cage lithium diffusion in LPSCI-II and LPSCI-III, respectively. The angle is between the Li-S bond and the z-axis. **k**, Free energy plot of concerted lithium diffusion in LPSCI-II. The predefined path is \mathbf{s} and the distance from the right path \mathbf{s} is \mathbf{z} .

The frustrated motion of Li ions, as quantified by the S_p , depends on the cooperativity of Li ions with their accommodating host. In argyrodite-type SSEs, rotation of the $[\text{PS}_4]^{3-}$ moiety is highly frequent (10^9 times per second),³³ A natural question is how the kinetics of moiety affects Li passing nearby. Taking all the $[\text{PS}_4]^{3-}$ units as a whole, which maintain rigid structures, we observe that the increased S_p is closely associated with the tilting of the tetrahedron in the anion framework. As illustrated in **Fig. 5a** and **5b**, the free energy profiles of the tilted tetrahedron at 300 K, with respect to its polar angle (θ) and azimuthal angle (ϕ), were derived from NNP-based molecular dynamics (NNMD) simulations. (**Supplementary Note 3**). LPSCI-I exhibits the most constraint tilt (**Supplementary Figure 31**), implying relatively frozen anion frames similar to its frozen LCSs. The Li-deficient LPSCI-III possesses a broader distribution of tilted states compared to LPSCI-I and II, suggesting more freedom of tetrahedrons in LPSCI-III which favors long-range lithium diffusion. With the presence of Si-centered tetrahedrons by Si substitution, LSPSCI shows the most extensively oriented tilt for both $[\text{SiS}_4]^{4-}$ and $[\text{PS}_4]^{3-}$ moieties (**Supplementary Figure 31**), suggesting the easiest rotation, and accounting for enhanced long-range lithium diffusion. At higher temperatures (600 K or 900 K), the decreased free energy barrier (**Supplementary Figure 32**) and broadening distribution of θ and ϕ angles in LPSCI-III and LSPSCI are more pronounced (**Supplementary Figures 33** and **34**).

The probabilistic distribution of tilt states enables the derivation of angularly resolved free energy. Thermodynamics analysis proves the connection of the

dynamics of anion frame and lithium diffusion (**Supplementary Note 2.4**, **Supplementary Table 5**, and **Supplementary Figures 35-40**). As depicted in **Fig. 5c**, the limited rotation and narrow distribution of tilting states of the $[\text{PS}_4]^{3-}$ units coincide with the poor σ of the LPSCI-I. In contrast, both LSPSCI and LPSCI-III exhibit high flexibility of anion framework rotation, ensuring a fast lithium diffusion, albeit via different mechanisms. Comparing LPSCI-II with LPSCI-III (**Fig. 5d** and **5e**), the unlocked rotation of $[\text{PS}_4]^{3-}$ is evident in LPSCI-III, characterized by a lower free energy across the whole configurational space. The presence of lithium vacancies and site disorder diversifies the local environment of $[\text{PS}_4]^{3-}$, resulting in a greater variety of tetrahedral configurations with lower transition barriers, thus enabling versatile lithium diffusion channels, as confirmed by the path entropy S_p . However, unlike LPSCI-III, the rotational free energy barrier of $[\text{PS}_4]^{3-}$ increases slightly in Si-doped case of LSPSCI (**Fig. 5f**) and up to ~ 300 kJ/mol for tetrahedrons substituted with Si ($[\text{SiS}_4]^{4-}$ or $[\text{SiS}_3\text{Cl}]^{3-}$) (**Fig. 5g** and **Supplementary Figure 41**). Although it appears that the increased free energy associated with tetrahedral distortion leads to limited entropy gain, the introduction of new types of anion-substituted tetrahedron creates new blocks with distinct distortion behaviors, ultimately forming versatile lithium diffusion channels.

We next examine the connection between configurational entropy (S_c) of anionic framework and path entropy of Li. The configurational disorder is assessed by the tetrahedron distortion (s_d), which measures the degree of similarity of the $[\text{PS}_4]^{3-}$ in comparison to a perfect tetrahedron (**Supplementary Note 4**), from which the S_c is defined as:³⁴

$$S_c = k_B \ln W(s_d) \quad (2)$$

where k_B is the Boltzmann constant and $W(s_d)$ is the number of possible configurations determined by the distribution of the s_d . As shown in **Fig. 5h**, the S_c increases from 31.07 J/mol/K (LPSCI-I), 32.53 J/mol/K (LPSCI-II), 34.18 J/mol/K (LSPSCI), to 34.45 J/mol/K (LPSCI-III), showing the enhanced disordering/distortion via doping or, surprisingly, simply inducing Li vacancy. On the other hand, the corresponding total path entropy, S_p , are derived for the Markov process of each structural variant. Notably, significant increases in S_p values are observed from 0.0

(LPSCI-I) to 30.06 (LPSCI-II), 45.91 (LSPSCI), and 50.15 (LPSCI-III). The S_p is positively correlated with the S_c , showing an implicit relationship between anionic backbone and Li transport. Systems with high S_c tend to exhibit richer diverse configurations which divert the Li pathway.

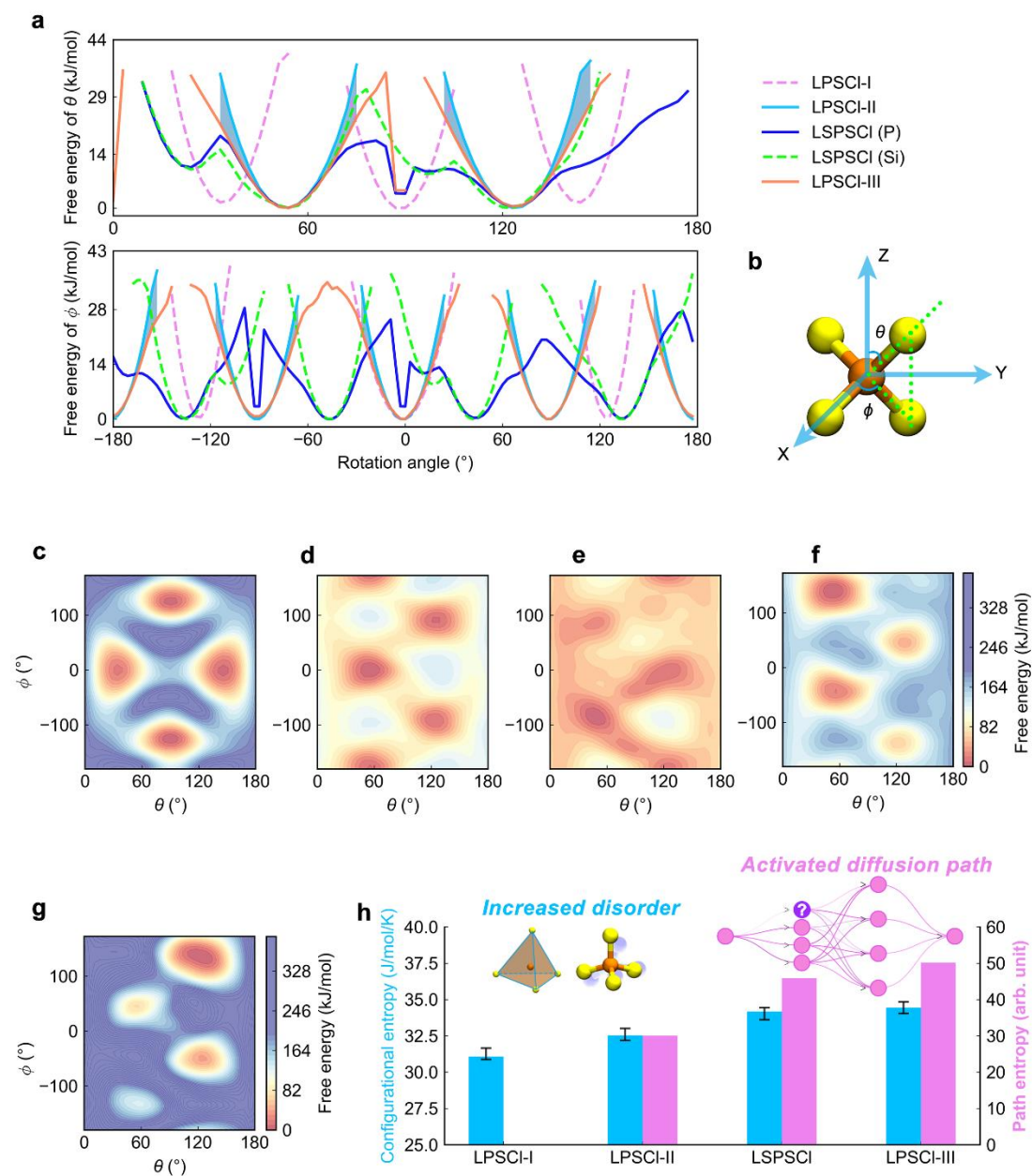


Fig. 5. Anion framework distortion analysis. **a**, Free energy plot of anion framework distortion characterized by azimuthal angles θ and ϕ of P(Si)-S bonds. The blue shadowed area denoted the free energy difference between LPSCI-II and LPSCI-III. **b**, Definition of the azimuthal angles θ and ϕ . **c-g**, Free energy plot of

rotation of P(Si)-S tetrahedral in angular space at 300 K for LPSCl-I, LPSCl-II, LPSCl-III, LSPSCl (P-S), and LSPSCl (Si-S), respectively. **h**, Comparison of configurational entropy of anionic framework and path entropy (with arbitrary unit) of Li of various phase of argyrodite-type SSEs.

We next show that a high S_p is accompanied with efficient Li conduction. As illustrated in **Fig. 6a**, the diffusion coefficient (D) of Li in Li-vacancy contained LPSCl-III (1.78×10^{-11} m²/s) and Si doped LSPSCl (1.14×10^{-12} m²/s) at 300 K are at least three orders of magnitude higher compared to pristine LPSCl-II, which is only 1.26×10^{-15} m²/s. The predicted D of LPSCl-III is reasonably consistent with experimental results (1.01×10^{-11} m²/s)²⁸. Notably, the corresponding σ , obtained through the Nernst-Einstein equation (please refer to **Supplementary Note 5, Supplementary Figure 42**), show excellent consistency with experiment findings, validating the accuracy of our NNP-based MD simulations. The σ values for LPSCl-II, LSPSCl, and LPSCl-III are 0.0018 mS/cm, in good agreement of solution-based experimental values ranging from 10^{-5} to 10^{-4} mS/cm²⁸, 1.49 mS/cm, and 22.39 mS/cm (higher than measured values of 9.4 mS/cm²⁸), respectively. It is noteworthy that the LPSCl-I shows an extremely low σ of about 2.96×10^{-9} mS/cm, which can be explained by almost zero S_p and a frozen discrete state-space according to our MSM prediction.

While ionic diffusion can be directly inferred from the atomic view of the S_p , the collective transport behaviours of a school of lithium ions govern the macroscopic performance. Here we introduce the metric of lithium softness to characterize the diffusive ability with regard to dynamic structural rearrangements. Lithium softness is established based on the relationship between lithium diffusion and its local environments (details in Methods section). Specifically, by considering the rearrangement described by the non-affine displacement D_{nd} of Li (**Fig. 6b**),³⁵ we classify the lithium rearrangement at high temperature (900 K), where the LCSs exhibit high disorder resembling glassy electrolytes, through both logistic regression and support vector machine (SVM) methods (**Supplementary Tables 6 and 7**). As expected, lithium atoms in LPSCl-I are the hardest with softness values around zero, indicating that the LCSs remain frozen even at high temperatures (**Fig. 6c and 6g**). In contrast, both LSPSCl (**Fig. 6e and 6i**) and LPSCl-III (**Fig. 6f and 6j**) exhibit softer

lithium atoms, with values exceeding 1.6, compared to LPSCI-II (**Fig. 6d** and **6h**) where the maximum is 1.0. This softness analysis proves again that both means of the reconstruction of the LCSs and the anion framework are effective entropy-driven design strategies. In depth analysis shows that vacancies and site disorder are more effective to soften the Li species than anion substitution which is limited by newborn “blocked sites” near the Si dopants.

Thermodynamics analysis through the direct construction of the 3D free energy surface of lithium diffusion further validates the rationality of lithium softness. The 3D energy surface at room temperature reveals a large volume of 3.375 nm³ per Li over an extended time scale of at least 5.0 nanoseconds, obtained by WTmetaD with lithium atomic position as the CV (**Supplementary Note 2.5, Supplementary Figure 43**). Consistent with the softness results, lithium atoms can migrate more freely in the order of LPSCI-I, LPSCI-II, LSPSCI, and LPSCI-III (**Fig. 6k** to **6n**). It’s worth noting that in LSPSCI, there are high diffusion barriers near to the blocked sites, as shown in both softness analysis and our MSMs. Hence, the addition of new elements in SSE may not always be effective. It is desirable that any dopants should be free of new blocked sites.

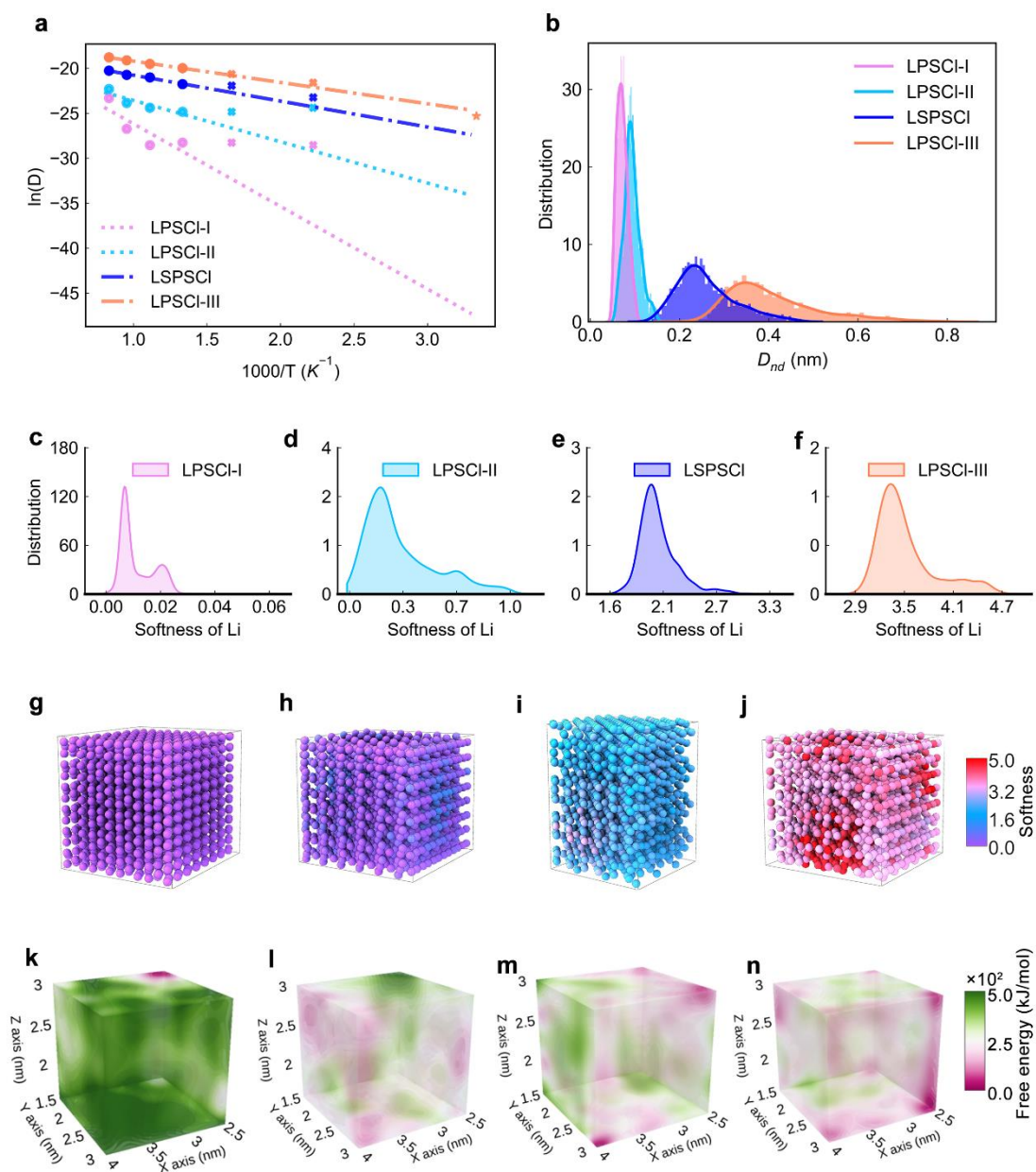


Fig. 6. Lithium superionic diffusion analysis. **a**, Logarithmic diffusion coefficients D of argyrodite-type SSEs as a function of temperature. The black star shows the experimental result of LPSCI-III from ref.²⁸. **b**, Non-affine displacement D_{nd} plot at 900 K. **c-f**, The lithium softness distributions of LPSCI-I, LPSCI-II, LSPSCI, and LPSCI-III, respectively. **g-j**, Visualization of the softness distributions in LPSCI-I, LPSCI-II, LSPSCI, and LPSCI-III, respectively. **k-n**, 3D free energy surfaces of LPSCI-I, LPSCI-II, LSPSCI, and LPSCI-III at room temperature, respectively.

Conclusion

The Arrhenius law pertains to entities undergoing thermally activated processes, where the rates of these processes are subject to enthalpy-entropy compensation. When the activating barrier is much greater than typical energy of heat bath ($k_B T$), according to multi-excitation entropy (MEE) theory¹³, multiple excitations from the heat bath are needed to surmount the large barrier, hence many ways are possible, thereby compensating entropy is generated. For shallow barriers (i.e., tens to hundreds of meV) with a relatively flat potential landscape, abnormal compensation disobeying MNR was noted¹⁶⁻¹⁸. This implies the existence of a different form of entropy, which we attribute here as “residual” entropy (ΔS_r), that governs the rate of process regardless of the barrier. Here by establishing the concept of the path entropy ΔS_p , we uncover the underlying principle governing the efficacy of entropy-driven design strategies in dense ionic transport systems. The ΔS_r , likely occurring with the exciting ΔS_p , reflects multipath under a shallow potential landscape. The idea of path entropy correlates the kinetics of particles with the activated states via multiple pathways. To this end, generation of disorder into anion framework is effective through diversifying transition channels with maximizing ΔS_p . This underscores the importance of pathway frustration³⁶ and likely accounts for several experimental observations: for instance, an exponential increase of σ with the content of Li in Garnet-type SSEs³⁷; an enhancement of σ by two orders of magnitude in the cubic phase of $\text{Li}_7\text{La}_3\text{Zr}_2\text{O}_{12}$ with disordered lithium-ion distribution compared to the ordered lithium-ion tetragonal phase³⁸; an increase in σ of polymer electrolytes through the reduction of crystallinity¹⁷, and doping enhanced liquid-like Li conduction³⁹, etc.

Notably, this scenario differs from the traditional concept in high-entropy alloys, where configurational entropy is utilized but remains largely unchanged over the time of interest. While the mechanical performance of high-entropy alloys relies on static configurational disordering, for ionic activated processes, kinetic properties associated with ion flux should invoke path entropy. The increase of the pre-factor and rate variables can thus be realized by promoting path entropy while simultaneously lowering the activation enthalpy, hopefully breaking the limitation of MNR. It will be particularly promising for screening systems with flattened energy landscape or frustrated lattice with low barriers while without compromising the pre-factor. We

envision that the concept of path entropy can be general and useful for analysing the formation of conducting channels and especially filaments in materials for neuromorphic computing.

Methods

AIMD simulation.

The first-principle calculations have been performed through CP2K software package.⁴⁰ The Perdew–Burke–Ernzerhof (PBE) generalized gradient approximation (GGA)⁴¹ with the double-zeta valence polarized basis set and Goedecker–Teter–Hutter pseudopotentials were adopted.⁴² The auxiliary plane wave basis set was truncated using a density cutoff of 500 Ry and the van der Waals (vdW) interactions were evaluated through Grimme D3 correction. A time step of 2.0 fs was used in all AIMD and WTmetaD simulations. The Nosé-Hoover thermostat and Martyna-Tobias-Klein barostat were used with coupling constants of 1.0 ps and 0.5 ps, respectively.

Identifying crystal structure of LPSCI-III ($\text{Li}_{5.5}\text{PS}_{4.5}\text{Cl}_{1.5}$).

The crystal structure of LPSCI-III was verified based on the experimental findings from ref.²⁸. All elements can be classified into Wyckoff sites as follows: Li (48h), P (4b), Cl (4a and 4c), S (4a, 4c, and 16 e). (see **Supplementary Figure 1**) To obtain the exact structure of $\text{Li}_{5.5}\text{PS}_{4.5}\text{Cl}_{1.5}$, which includes lithium vacancies and site mixture of Cl/S at Wyckoff 4a and 4c sites, we initially employed an enumerative approach to generate possible structures consistent with the site positions. Over a range of cell sizes from 1 to 4, we generated more than 1000 initial structures through enumeration. For all those structures, we performed first-principles calculations (Please refer to **Supplementary Figure 2**). Next, we employed cluster expansion (CE) to identify the most stable candidates among the target structures (**Supplementary Figures 2 and 3**).

The atomic configuration of the LPSCI-III can be represented by a string of occupation variables, $\{\zeta_1, \zeta_2, \dots, \zeta_n\}$, where the ζ_n represents the atomic species occupying the n^{th} site in an N -site supercell. The lattice model of the atomic configuration can be written as a sum of cluster interaction functions:⁴³

$$H(\zeta) = \sum_{S \subseteq [N]} H_S(\zeta_S) \quad (3)$$

In our CE model, $[N]$ is the set of all site indices, and ζ_S is the set of all occupation variables for sites in a cluster S . The CE model includes pairs of sites separated by less than 6 Å, triples with points less than 5 Å, quadruplets 4 Å apart, and quintuplets 4 Å apart, resulting in a total of 27 correlation functions. Initially, we selected 340 possible candidates to create the CE model, achieving a final mean squared error of 100.05 meV/prim (primitive cell) in predicting the energies. Subsequently, using this model, we predicted around 1100 structures of LPSCI-III as candidates. We then filtered more than ten energetically favorable structures included for NNP training.

NNP training.

The initial training datasets were prepared through AIMD simulations conducted using the CP2K software package. These simulations were carried out for all four argyrodite-type solid-state electrolytes across temperature ranges from 300 K to 1500 K. Subsequently, neural network-based potentials were trained using the Deep Potential Smooth Edition (DeepPot-SE)⁴⁴, which incorporates both angular and radial information from atomic configurations. The detailed active learning for MLP training is outlined as follows (**Supplementary Figure 4**): (1) For each type of SSE, we conducted 10.0 ps of AIMD simulations at temperatures of 300 K, 600 K, 900 K, 1200 K, and 1500 K, and a pressure of 1 atm under the NPT ensemble. Subsequently,

for each NPT simulation, we selected two frames as candidates for the next MD simulation under the NVT ensemble. Under the NVT ensemble, we employed the On-the-fly Probability Enhanced Sampling (OPES) method⁴⁵ with multithermal sampling to enrich the dataset. The internal energy (U) of the system was used for defining the CV by Δu defined as

$$\Delta u_{\beta'} = (\beta' - \beta)U \quad (4)$$

where $\beta = 1/(k_B T)$ and k_B is Boltzmann constant, β' is the inverse thermodynamic temperature to be sampled. For the ten AIMD simulations under the NVT ensemble, we sampled temperature ranges $\{(0 \text{ to } 600 \text{ K}), (300 \text{ to } 900 \text{ K}), (600 \text{ to } 1200 \text{ K}), (900 \text{ to } 1500 \text{ K})\}$ using multithermal simulations. Each simulation was run for at least 5.0 ps under the NVT ensemble. Note for LPSCI-III, we conducted five MD simulations under the NVT ensemble for all ten candidates predicted to be stable by our CE model.

(2) Training the NNP using DeepPot-SE involved extracting energies and forces from the previous MD trajectories. The detailed parameters used for training are provided in **Supplementary Table 1**. (3) Based on the initial NNP models, a series of NNMD simulations were conducted under both NVT and NPT ensembles using enhanced OPES multithermal-multibaric (MTB). With OPES-MTB, the simulations were biased across a range of temperatures (300 K to 1200 K) and pressures (0.90 atm to 1.10 atm). Candidate configurations were identified based on model deviations of force falling within the range of 0.15 to 0.25 eV/Å. (4) The energies and forces of these candidates were calculated using DFT, and the resulting data were added to the initial training sets. (5) With the enriched dataset, we iteratively train the new dataset to optimize the model and improve its accuracy. This iterative training process involves updating the neural network potential model based on the new data, refining the

model parameters, and repeating the training process until the desired level of accuracy (greater than 99%) is achieved.

To validate the NNPs, we compare the mean absolute errors and radial distribution functions of lithium between the results obtained from AIMD calculations and the predictions made by the NNPs. (**Supplementary Table 2, Supplementary Figures 5 to 9**)

MSM construction.

The construction steps of our MSM in studying the lithium diffusion are as follows (**Supplementary Figure 12**): MD simulations were performed under the NVT ensemble at different temperatures (e.g., 300 K, 600 K, and 900 K). We then define the LCS of each SSE structure. The second step was discretizing of LCS. Lithium ions in each LCS were uniquely assigned into distinct discretized segment states. Discretization was performed based on the geometric features of the LCS, such as bond angles and distances between lithium ions and coordination centers (e.g., sulfur, phosphorus, chlorine). A lithium-ion hopping trajectory can thus be modeled as a chain of random variables $H_1, H_2, \dots, H_t \dots$ over discrete time moments (t) with H_t being randomly one state in state space $\{X_i\}$. Within the framework of the Markov method, the probability distribution (p) of H_{t+1} variable at the time moment $t+1$ is assumed to depend only on the variable at the prior moment (i.e. t), thus we have:

$$p(H_{t+1}|H_t, H_{t-1}, \dots, H_2, H_1) = p(H_{t+1}|H_t) \quad (5)$$

Therefore, the time-dependent trajectories of a group of Li atoms are equivalent to a time series of probabilistic variables evolving from an initial distribution $p(0)$. The

vector of probability density function $\mathbf{p}(t)$ of all the states dictated by the LCSs, evolving over a time interval τ (lag time), is represented as:

$$\mathbf{p}(t + \tau)^T = \mathbf{p}(t)^T \mathbf{T}(\tau) \quad (6)$$

and its explicit form expressed as

$$\mathbf{p}_j(t + \tau) = \sum_{i=1}^n \mathbf{p}_i(t) \mathbb{P}(x(t + \tau) \in X_j \mid x(t) \in X_i) \quad (7)$$

where $\mathbf{T}(\tau)$ is the transition probability matrix (TPM) with its component \mathbf{T}_{ij} being the transition probability between two basis X_i and X_j over τ , and its eigenvectors offer insights into the population flux of the dynamic process of lithium site hopping. Particularly, its eigenvalues (λ_i) denote the timescales of these dynamic processes, which can be depicted in implied time scales (ITS):

$$\text{ITS}_i(\tau) = -\frac{\tau}{\ln \lambda_i(\tau)} \quad (8)$$

where $i = 1, 2, 3, 4, \dots$ represents i th eigenvalue of the $\mathbf{T}(\tau)$. To ensure the reduced state space remains memoryless (or reducing history effect) in capturing the kinetics of lithium hopping, we select a lag time $\tau = 600 \text{ steps}$ (12.0 picosecond). Each LCS in the trajectory contributes to the construction of the MSM, helping to reduce both random and systematic errors in the model. To assess the validity and equality of the lithium hopping MSMs, the Chapman-Kolmogorov (C-K) test was employed. This test evaluates the consistency of transition probabilities between different discrete states over time (**Supplementary Figures 44 to 46**).

Calculation of lithium flux.

We implement TPT²⁹ to analyze the reactive trajectories of the lithium transition. From TPT, we analyze the flux of the lithium that moves from different states – the hopping rate. The lithium jumping process is modeled on the countable state-space S with rate matrix $L = (l_{ij})_{i,j \in S}$:

$$\begin{cases} l_{ij} \geq 0 & \forall i, j \in S, i \neq j \\ \sum_{j \in S} l_{ij} = 0 & \forall i \in S \end{cases} \quad (9)$$

where l_{ij} represents the process jump from state i to state j . Given the initial state of lithium at i and the final migrated state at j , TPT can compute the reactive flux between any two nonempty, disjoint subsets (e.g. A and B) of the state-space S . The reactive trajectory P , the set of all the ordered sequence P_n generated from the n th transition between initial state A and end state B, is defined as:

$$P = \bigcup_{n \in \mathbb{Z}} P_n \quad (10)$$

Then for this reactive trajectories P , the discrete forward committor $q^+ = (q_i^+)_{i \in S}$ is defined as the probability that the process starting in $i \in S$ will first evolve toward B rather than A. Similarly, the probability of process arriving in state i last came from A rather than B is the backward committor $q^- = (q_i^-)_{i \in S}$. We can calculate the probability current of reactive trajectories P :²⁹

$$f_{ij}^{AB} = \begin{cases} \pi_i q_i^- l_{ij} q_j^+, & \text{if } i \neq j \\ 0, & \text{otherwise} \end{cases} \quad (11)$$

where π is the unique stationary distribution. The flux between different states is conserved through:

$$\sum_{j \in S} (f_{ij}^{AB} - f_{ji}^{AB}) = 0 \quad \forall i \in (A \cup B)^c \quad (12)$$

Free energy calculation through WTmetaD.

We utilize WTmetaD simulations to investigate lithium diffusion through the metadynamics method. Various CVs are designed to capture the migration behaviors in distinct local environments. For specifics on CV design (**Supplementary Figures 23, 26, and 29**) and simulation parameters (**Supplementary Table 5**), please refer to **Supplementary Note 2**.

Analysis of lithium softness.

The lithium atoms were categorized based on their D_{nd} values. The training dataset was derived from four NNMD trajectories conducted under NVT ensemble at 900 K of LPSCI-I, LPSCI-II, LPSCI-III, and LSPSCI, each consisting 4608, 3744, 3600, and 3600 atoms, respectively. The lithium's local environment is characterized using the radial density properties of the neighborhood (G):

$$G(i; \mu) = \sum_j \exp\left(\frac{-(R_{ij} - \mu)^2}{L^2}\right) \quad (13)$$

where L is the thickness of the shell, and μ is the constant of Gaussian functions centered around μ . Here we set 1 for L and μ is from 0.3 - 5.0 with an increment of 0.1. We then use two algorithms – SVM²³ and logistic regression²⁴ to classify the lithium atoms using scikit-learn and Tensorflow2. The model parameters and accuracies are presented in **Supplementary Table 6** and **Supplementary Table 7** for SVM and logistic regression models, respectively.

Code availability

The sample code to perform the analysis is available at <https://github.com/DXiming/entropy-dirven-SSE>

References

- 1 Deng, J., Bae, C., Denlinger, A. & Miller, T. Electric vehicles batteries: requirements and challenges. *Joule* **4**, 511-515 (2020).
- 2 Park, M., Zhang, X., Chung, M., Less, G. B. & Sastry, A. M. A review of conduction phenomena in Li-ion batteries. *J. Power Sources* **195**, 7904-7929 (2010).
- 3 Bachman, J. C. *et al.* Inorganic solid-state electrolytes for lithium batteries: mechanisms and properties governing ion conduction. *Chem. Rev.* **116**, 140-162 (2016).
- 4 Manthiram, A., Yu, X. & Wang, S. Lithium battery chemistries enabled by solid-state electrolytes. *Nat. Rev. Mater.* **2**, 16103 (2017).
- 5 Zhang, Z., Roy, P.-N., Li, H., Avdeev, M. & Nazar, L. F. Coupled cation–anion dynamics enhances cation mobility in room-temperature superionic solid-state electrolytes. *J. Am. Chem. Soc.* **141**, 19360-19372 (2019).
- 6 Adelstein, N. & Wood, B. C. Role of dynamically frustrated bond disorder in a Li⁺ superionic solid electrolyte. *Chem. Mat.* **28**, 7218-7231 (2016).
- 7 Kraft, M. A. *et al.* Influence of Lattice Polarizability on the Ionic Conductivity in the Lithium Superionic Argyrodites Li(6)PS(5)X (X = Cl, Br, I). *J. Am. Chem. Soc.* **139**, 10909-10918 (2017).
- 8 Krauskopf, T., Pompe, C., Kraft, M. A. & Zeier, W. G. Influence of Lattice Dynamics on Na⁺Transport in the Solid Electrolyte Na₃PS₄–xSex. *Chem. Mat.* **29**, 8859-8869 (2017).
- 9 Meyer, W. & Neldel, H. Zeitschr. f. techn. *Physik* **12**, 588 (1937).
- 10 Exner, O. Concerning the isokinetic relationship. *Nature* **201**, 488-490 (1964).
- 11 Blackadder, D. & Hinshelwood, C. The kinetics of the decomposition of the addition compounds formed by sodium bisulphite and a series of aldehydes and ketones. Part II. General discussion of energy–entropy relations. *Journal of the Chemical Society (Resumed)*, 2728-2734 (1958).
- 12 Wert, C. & Zener, C. Interstitial atomic diffusion coefficients. *Phys. Rev.* **76**, 1169 (1949).
- 13 Yelon, A., Movaghar, B. & Crandall, R. Multi-excitation entropy: its role in thermodynamics and kinetics. *Rep. Prog. Phys.* **69**, 1145 (2006).

- 14 Fox, J. M., Zhao, M., Fink, M. J., Kang, K. & Whitesides, G. M. The molecular origin of enthalpy/entropy compensation in biomolecular recognition. *Annual Review of Biophysics* **47**, 223-250 (2018).
- 15 Du, P., Zhu, H., Braun, A., Yelon, A. & Chen, Q. Entropy and Isokinetic Temperature in Fast Ion Transport. *Adv. Sci.* **11**, 2305065 (2024).
- 16 Di Stefano, D. *et al.* Superionic diffusion through frustrated energy landscape. *Chem* **5**, 2450-2460 (2019).
- 17 Zhao, Q., Stalin, S., Zhao, C.-Z. & Archer, L. A. Designing solid-state electrolytes for safe, energy-dense batteries. *Nat. Rev. Mater.* **5**, 229-252 (2020).
- 18 Almond, D. P. & West, A. R. Entropy effects in ionic conductivity. *Solid State Ion.* **18-19**, 1105-1109 (1986).
- 19 Linert, W. & Jameson, R. The isokinetic relationship. *Chem. Soc. Rev.* **18**, 477-505 (1989).
- 20 Krauskopf, T. *et al.* Comparing the descriptors for investigating the influence of lattice dynamics on ionic transport using the superionic conductor Na₃PS_{4-x}Se_x. *J. Am. Chem. Soc.* **140**, 14464-14473 (2018).
- 21 Ekroot, L. & Cover, T. M. The entropy of Markov trajectories. *IEEE Transactions on Information Theory* **39**, 1418-1421 (1993).
- 22 Miller, A. & Abrahams, E. Impurity Conduction at Low Concentrations. *Phys. Rev.* **120**, 745-755 (1960).
- 23 Schoenholz, S. S., Cubuk, E. D., Sussman, D. M., Kaxiras, E. & Liu, A. J. A structural approach to relaxation in glassy liquids. *Nat. Phys.* **12**, 469-471 (2016).
- 24 Chen, Z., Du, T., Christensen, R., Bauchy, M. & Smedskjaer, M. M. Deciphering How Anion Clusters Govern Lithium Conduction in Glassy Thiophosphate Electrolytes through Machine Learning. *ACS Energy Lett.*, 1969-1975 (2023).
- 25 Kato, Y. *et al.* High-power all-solid-state batteries using sulfide superionic conductors. *Nat. Energy.* **1**, 16030 (2016).
- 26 Feng, X. *et al.* Review of modification strategies in emerging inorganic solid-state electrolytes for lithium, sodium, and potassium batteries. *Joule* **6**, 543-587 (2022).
- 27 Famprakis, T., Canepa, P., Dawson, J. A., Islam, M. S. & Masquelier, C. Fundamentals of inorganic solid-state electrolytes for batteries. *Nat. Mater.* **18**, 1278-1291 (2019).
- 28 Adeli, P. *et al.* Boosting Solid-State Diffusivity and Conductivity in Lithium Superionic Argyrodites by Halide Substitution. *Angew. Chem. Int. Ed.* **58**, 8681-8686 (2019).

- 29 Metzner, P., Schütte, C. & Vanden-Eijnden, E. Transition Path Theory for Markov Jump Processes. *Multiscale Modeling & Simulation* **7**, 1192-1219 (2009).
- 30 Haaks, M., Martin, S. W. & Vogel, M. Relation of short-range and long-range lithium ion dynamics in glass-ceramics: Insights from ^7Li NMR field-cycling and field-gradient studies. *Phys. Rev. B* **96** (2017).
- 31 Hunter, J. J. The computation of the mean first passage times for Markov chains. *Linear Algebra and its Applications* **549**, 100-122 (2018).
- 32 Jalem, R. *et al.* Concerted Migration Mechanism in the Li Ion Dynamics of Garnet-Type $\text{Li}_7\text{La}_3\text{Zr}_2\text{O}_{12}$. *Chem. Mat.* **25**, 425-430 (2013).
- 33 Hanghofer, I., Gadermaier, B. & Wilkening, H. M. R. Fast Rotational Dynamics in Argyrodite-Type $\text{Li}_6\text{PS}_5\text{X}$ (X: Cl, Br, I) as Seen by ^{31}P Nuclear Magnetic Relaxation—On Cation–Anion Coupled Transport in Thiophosphates. *Chem. Mat.* **31**, 4591-4597 (2019).
- 34 Jaynes, E. T. Gibbs vs Boltzmann entropies. *American Journal of Physics* **33**, 391-398 (1965).
- 35 Cubuk, E. D. *et al.* Identifying structural flow defects in disordered solids using machine-learning methods. *Phys. Rev. Lett.* **114**, 108001 (2015).
- 36 Wood, B. C. *et al.* Paradigms of frustration in superionic solid electrolytes. *Philosophical Transactions of the Royal Society A: Mathematical, Physical and Engineering Sciences* **379**, 20190467 (2021).
- 37 Wang, C. *et al.* Garnet-Type Solid-State Electrolytes: Materials, Interfaces, and Batteries. *Chem. Rev.* **120**, 4257-4300 (2020).
- 38 Murugan, R., Thangadurai, V. & Weppner, W. Fast lithium ion conduction in garnet-type $\text{Li}_7\text{La}_3\text{Zr}_2\text{O}_{12}$. *Angew. Chem. Int. Ed.* **46**, 7778-7781 (2007).
- 39 Wu, J.-F. *et al.* Liquid-Like Li-Ion Conduction in Oxides Enabling Anomalously Stable Charge Transport across the Li/Electrolyte Interface in All-Solid-State Batteries. *Adv. Mater.* **35**, 2303730 (2023).
- 40 VandeVondele, J. *et al.* Quickstep: Fast and accurate density functional calculations using a mixed Gaussian and plane waves approach. *Comput. Phys. Commun.* **167**, 103-128 (2005).
- 41 Perdew, J. P., Burke, K. & Ernzerhof, M. Generalized Gradient Approximation Made Simple. *Phys. Rev. Lett.* **77**, 3865-3868 (1996).
- 42 Goedecker, S., Teter, M. & Hutter, J. Separable dual-space Gaussian pseudopotentials. *Phys. Rev. B* **54**, 1703-1710 (1996).
- 43 Barroso-Luque, L. *et al.* Cluster expansions of multicomponent ionic materials: Formalism and methodology. *Phys. Rev. B* **106** (2022).
- 44 Zhang, L. F., Han, J. Q., Wang, H., Car, R. & Weinan, E. Deep Potential Molecular Dynamics: A Scalable Model with the Accuracy of Quantum Mechanics. *Phys. Rev. Lett.* **120**, 6 (2018).

- 45 Invernizzi, M. & Parrinello, M. Rethinking Metadynamics: From Bias Potentials to Probability Distributions. *J. Phys. Chem. Lett.* **11**, 2731-2736 (2020).

Supplementary Data

Unlocking the Ion Migration in Solid-State Electrolytes via Path Entropy

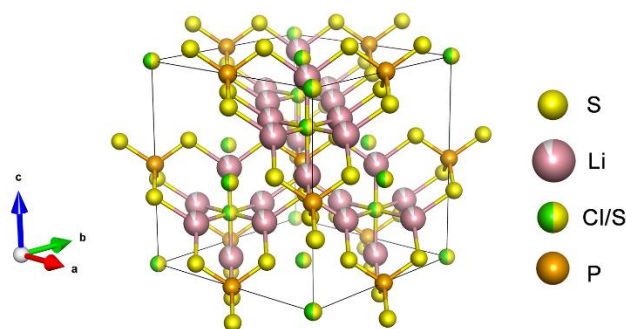
This file includes:

Supplementary Figures 1-46

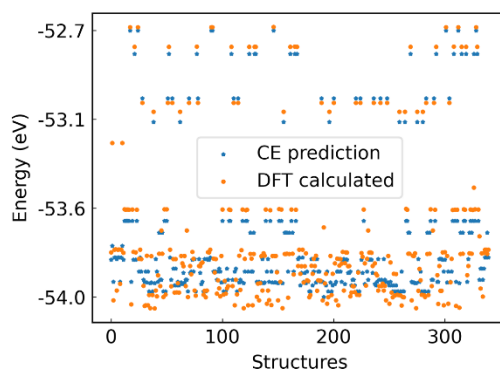
Supplementary Tables 1-7

Supplementary Notes 1-5

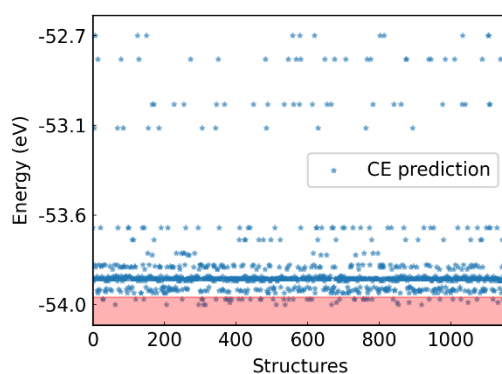
Supplementary References



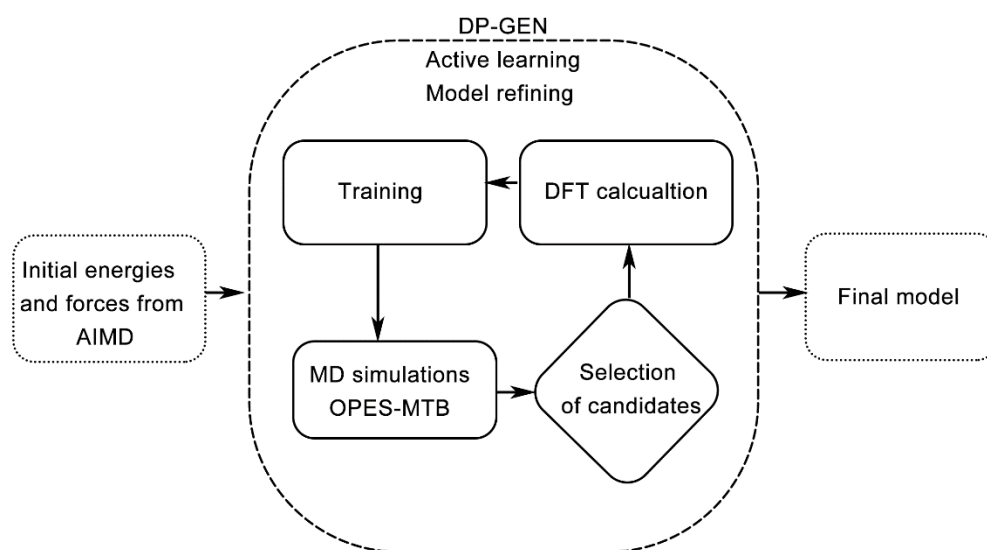
Supplementary Figure 1. The site positions of experimentally validated LPSCI-III ($\text{Li}_{5.5}\text{PS}_{4.5}\text{Cl}_{1.5}$)¹. All elements can be classified into Wyckoff sites as follows: Li (48h), P (4b), Cl (4a and 4c), S (4a, 4c, and 16 e). Over a range of cell sizes from 1 to 4, we generated more than 1000 initial structures using the Pymatgen enumeration package^{2,3} to find the most stable structure of LPSCI-III, which includes lithium vacancies and Cl/S site disorder at Wyckoff 4a and 4c sites.



Supplementary Figure 2. Construction of the cluster expansion model of LPSCI-III. By calculating more than 340 initial structures, we construct our cluster expansion (CE) model through the Statistical Mechanics on Lattices (smol) package⁴. For all those structures, first-principles calculations are performed through the Vienna ab initio simulation package (VASP)⁵ with the projector augmented wave (PAW) method. The exchange-correlation energy is computed within the GGA, employing the PBE functional.⁶ Additionally, the DFT-D3 functional with Grimme correction is utilized to account for weak vdW interactions.⁷ The calculations are conducted with an energy cutoff of 450 eV and an energy convergence criterion of 10^{-4} eV.

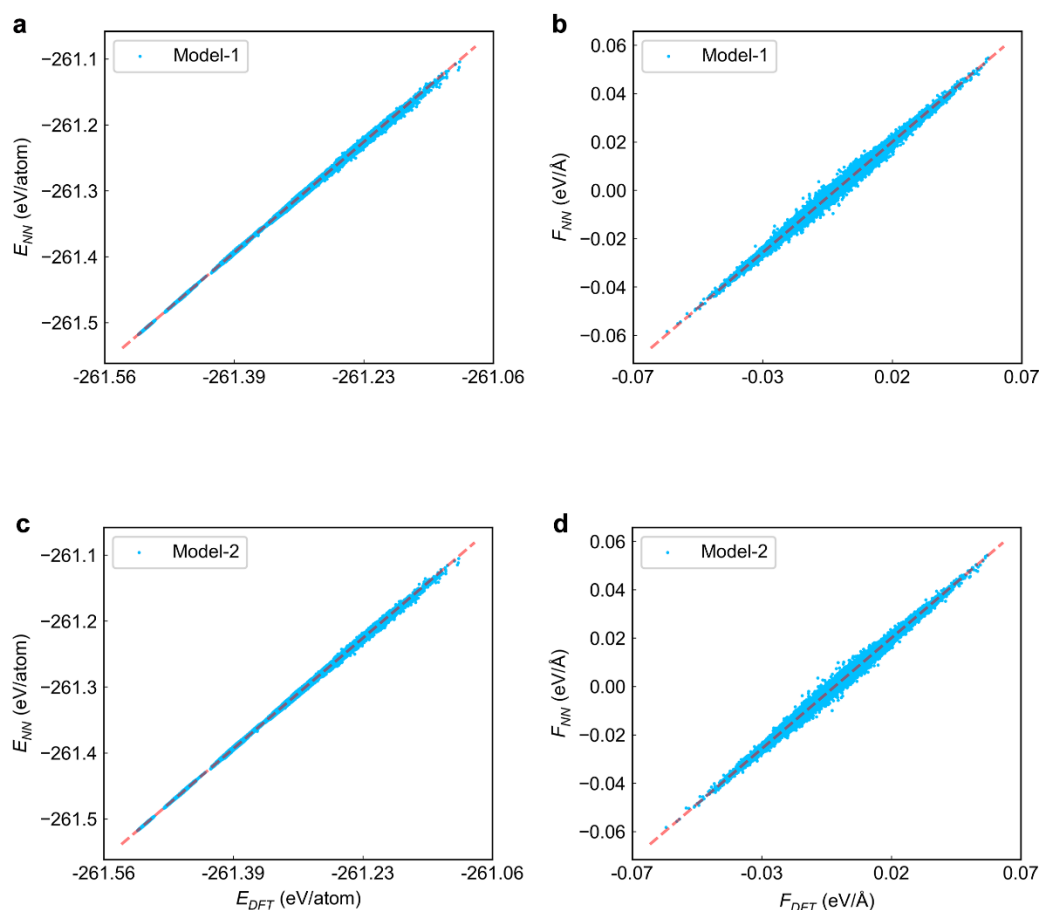


Supplementary Figure 3. Selection of structure candidates of LPSCI-III. The candidates search using the CE model. The red area shows the possible candidates that are stable. We then select 10 of the most stable candidates from the red area among more than 1000 initial structures.

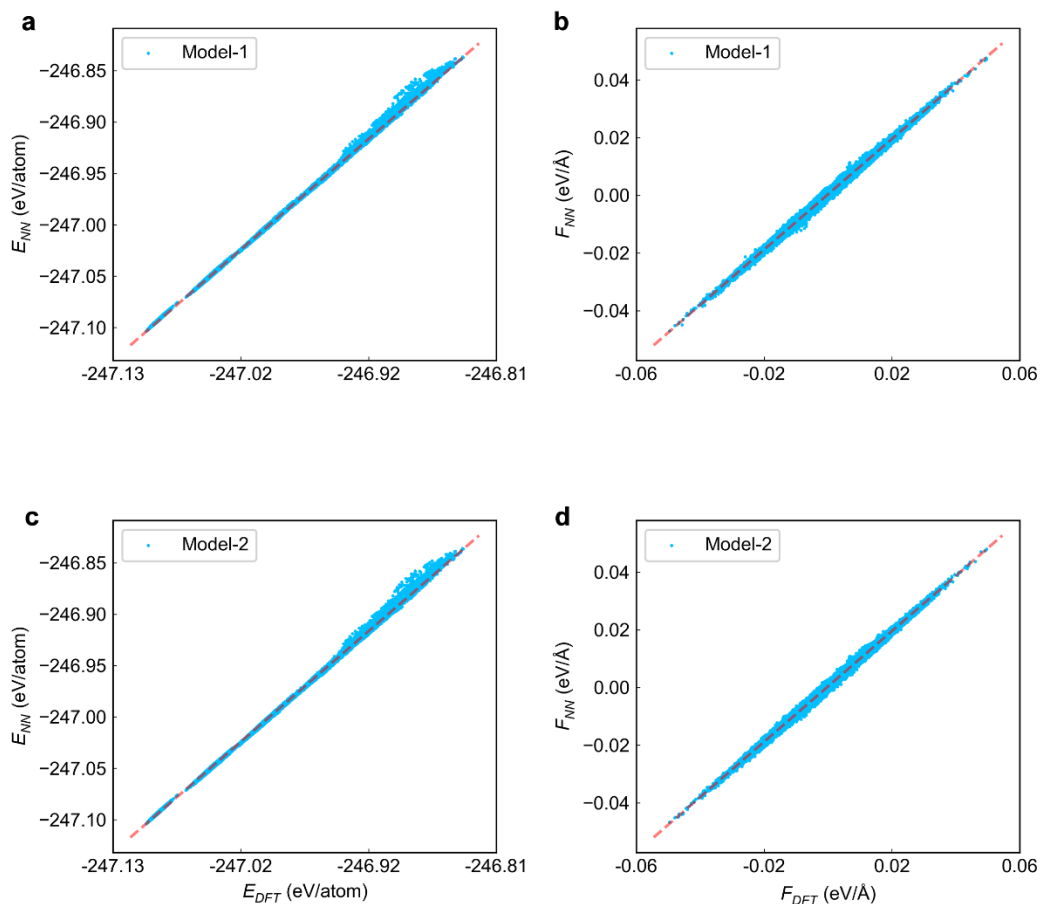


Supplementary Figure 4. Workflow in training neural-network potentials (NNPs). The initial training datasets were prepared through AIMD simulations conducted using the CP2K software package. These simulations were carried out for all four argyrodite-type solid-state electrolytes across temperature ranges from 300K to 1500K, employing OPES-MTB (On-the-fly probability enhanced sampling with multithermal and multibaric energy collective variable) simulations using plumed^{8,9}. Subsequently, neural network-based potentials were trained using the Deep Potential

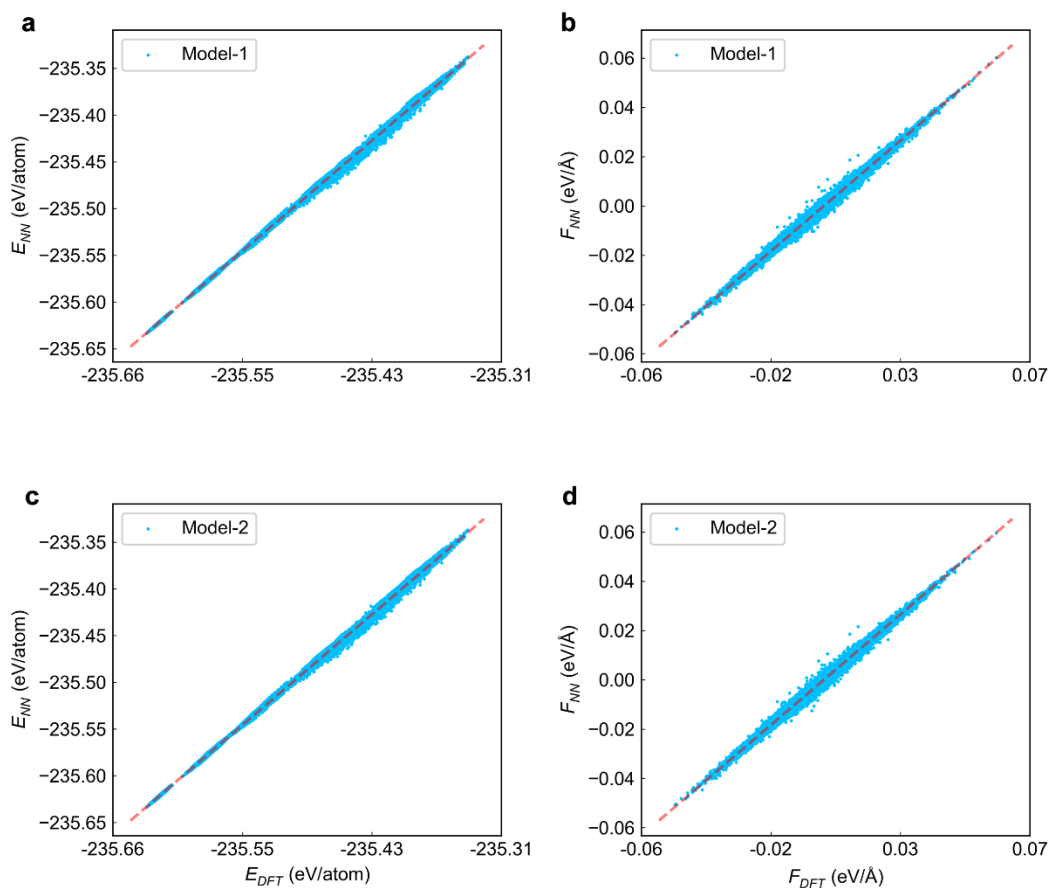
Smooth Edition (DeepPot-SE)¹⁰, which incorporates both angular and radial information from atomic configurations. The DeepPot-SE was constructed using the DeepMD-kit package¹¹. Active learning was employed for MLP training, utilizing the dp-gen package¹².



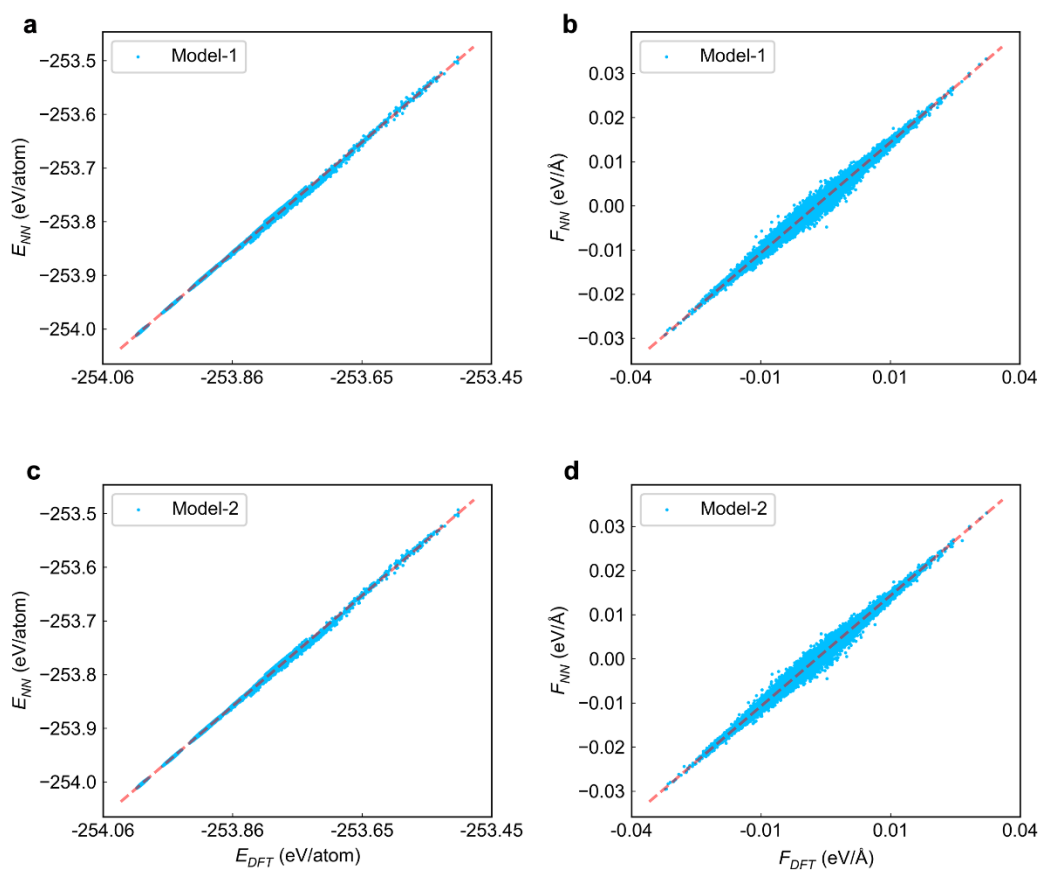
Supplementary Figure 5. Evaluation of the NNP of LPSCI-I. **a-b**, The differences of energies and forces between DFT calculation and NNP from model-1, respectively. **c-d**, The differences of energies and forces between DFT calculation and NNP from model-2, respectively. The red dotted line represents the energy/force calculated from DFT.



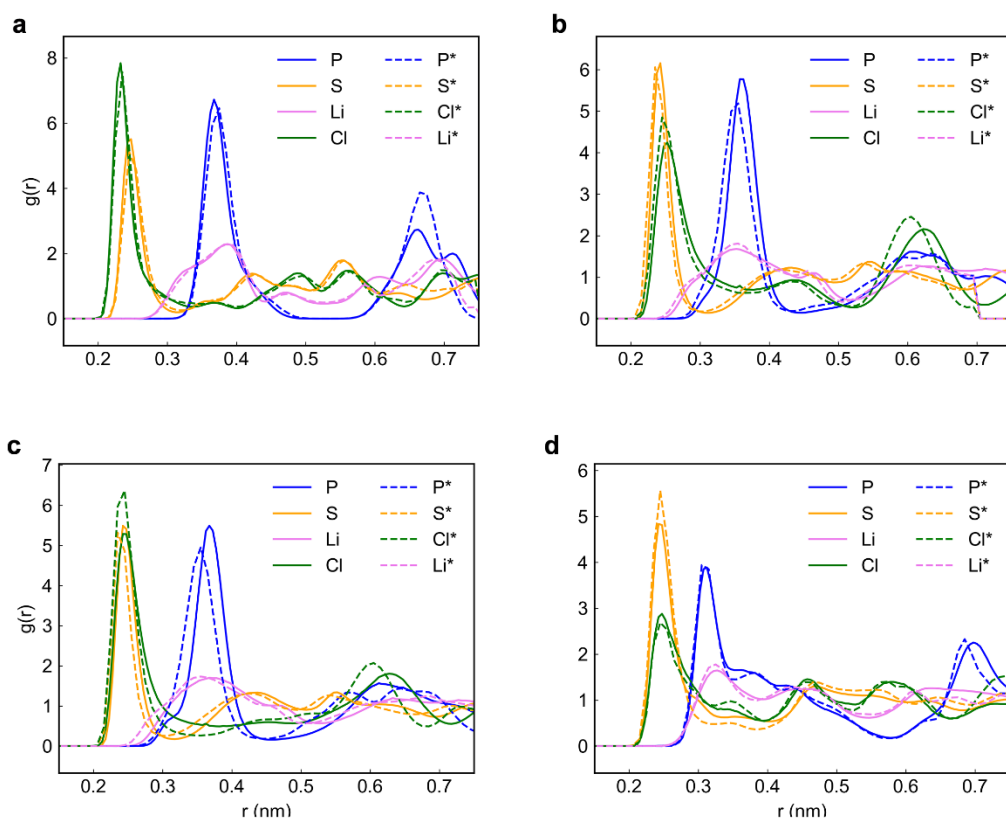
Supplementary Figure 6. Evaluation of the NNP of LPSCI-II. **a-b**, The differences of energies and forces between DFT calculation and NNP from model-1, respectively. **c-d**, The differences of energies and forces between DFT calculation and NNP from model-2, respectively. The red dotted line represents the energy/force calculated from DFT.



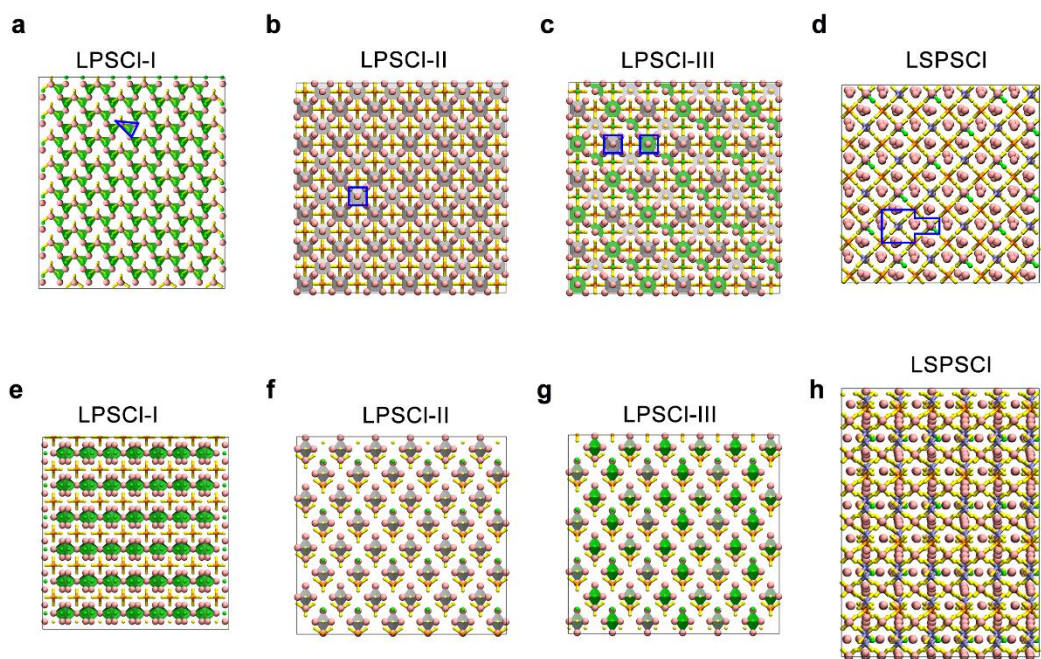
Supplementary Figure 7. Evaluation of the NNP of LPSCI-II. **a-b**, The differences of energies and forces between DFT calculation and NNP from model-1, respectively. **c-d**, The differences of energies and forces between DFT calculation and NNP from model-2, respectively. The red dotted line represents the energy/force calculated from DFT.



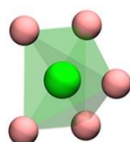
Supplementary Figure 8. Evaluation of the NNP of LPSCI-III. **a-b**, The differences of energies and forces between DFT calculation and NNP from model-1, respectively. **c-d**, The differences of energies and forces between DFT calculation and NNP from model-2, respectively. The red dotted line represents the energy/force calculated from DFT.



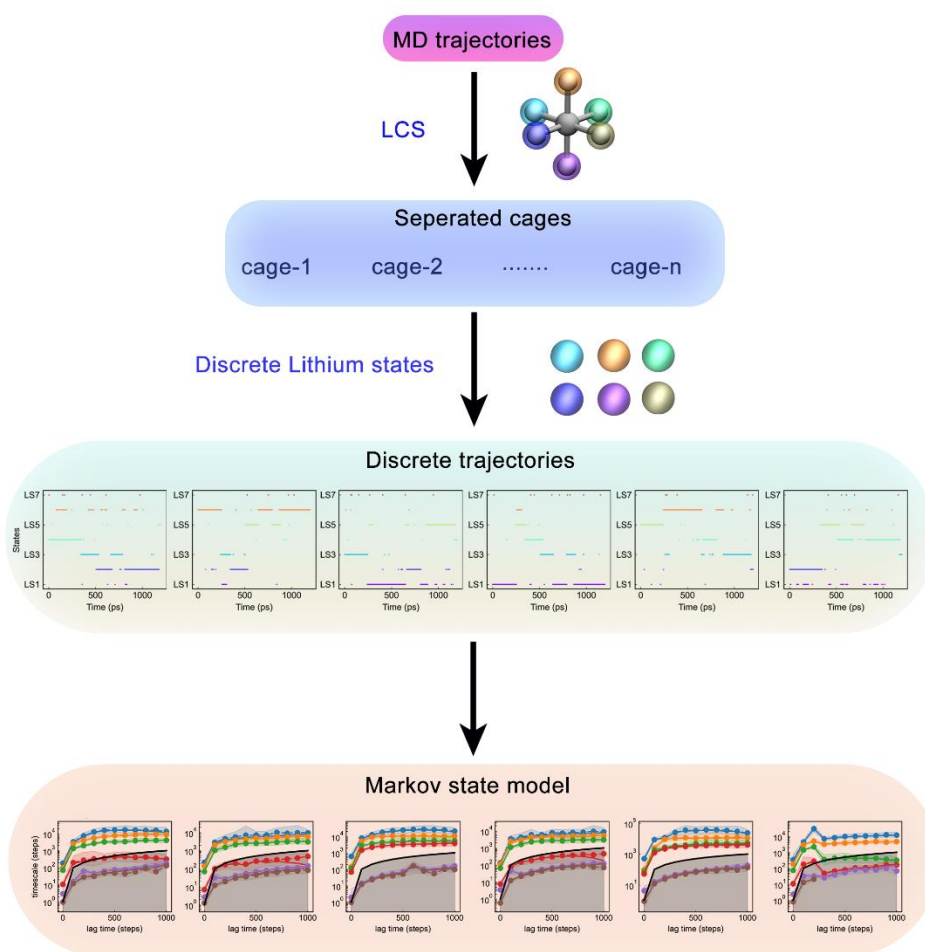
Supplementary Figure 9. Radial distribution function plot of Lithium with P, S, Li, and Cl elements at 300 K under NVT ensemble. a, LPSCI-I, b, LPSCI-II, c, LSPSCI, and d, LPSCI-III. The dotted and solid lines represent the calculation from DFT and NNPs, respectively.



Supplementary Figure 10. Crystal structures of argyrodite-type SSEs. Top (a-d) and side (e-h) view of structures of LPSCI-I, LPSCI-II, LPSCI-III, LSPSCI. The Li, P, S, and Cl atoms are colored pink, orange, yellow, and green. The lithium coordination shells (LCSs) are denoted with blue lines.

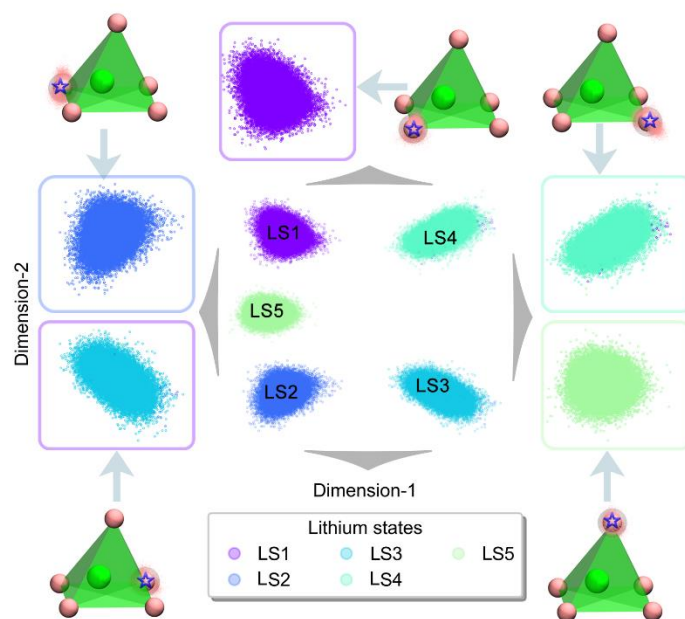


Supplementary Figure 11. Lithium coordination shell (LCS) of LPSCI-I.

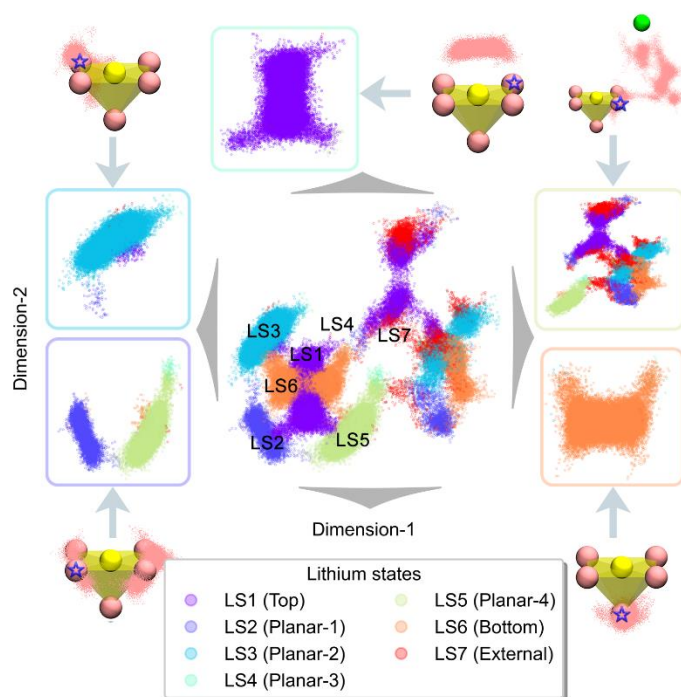


Supplementary Figure 12. The schematic diagram of the construction of MSMs.

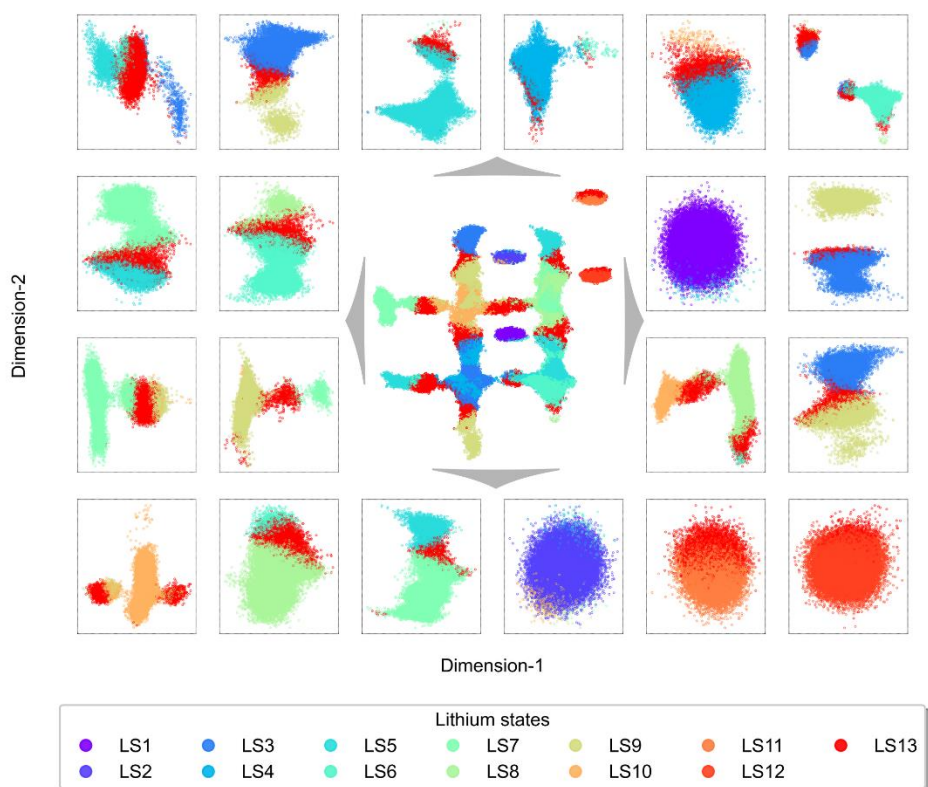
MD simulations are performed under the NVT ensemble at different temperatures (e.g., 300 K, 600 K, and 900 K) through LAMMPS¹³ with i-Pi¹⁴ software. We then define the LCS of each type of SSE. The second step is discretization of the lithium states in every LCS. The lithium ions in each LCS are discretized into distinct states. Discretization is performed based on the geometric features of the LCS, such as bond angles and distances between lithium ions and coordination centers (e.g., sulfur, phosphorus, chlorine). Using the discretized trajectories, the final MSM model is constructed¹⁵. Each LCS in the trajectory contributes to the construction of the MSM, helping to reduce both random and systematic errors in the model.



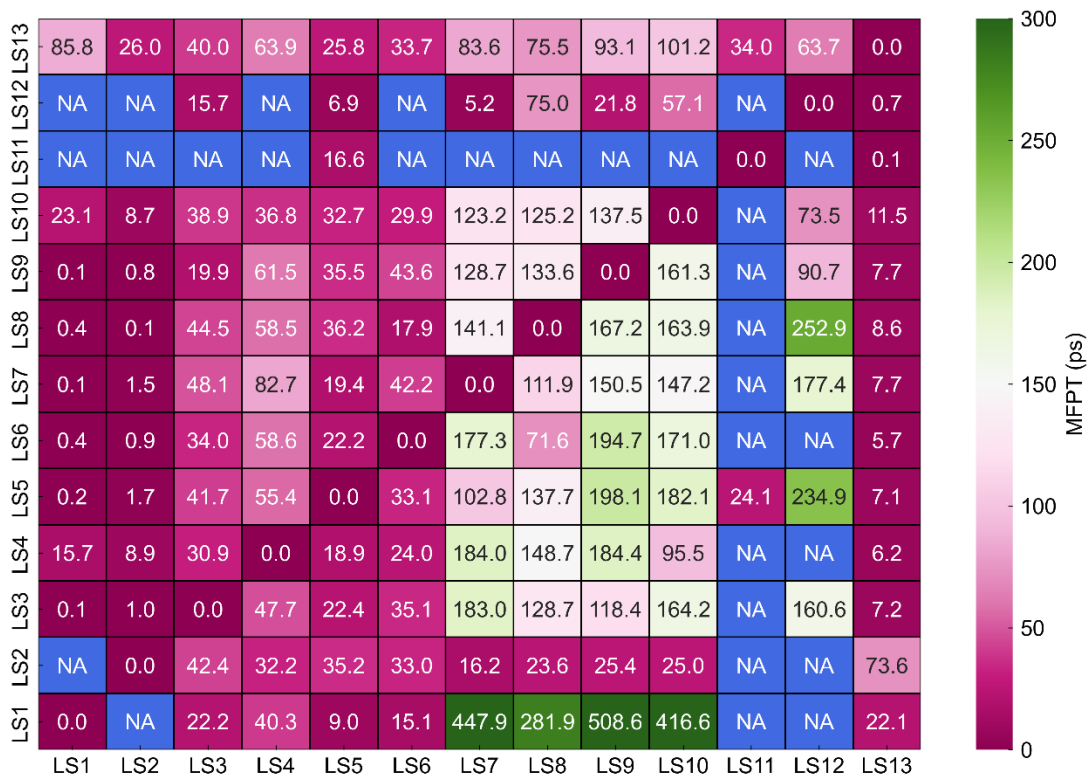
Supplementary Figure 13. Projected discrete lithium trajectories from 3D space in one LCS of LPSCI-I. The lithium diffusion paths in this LCS, and lithium states (LS) are classified with different colors. The initial position of the lithium atom is denoted with star and the trajectories in 3D space are coloured pink.



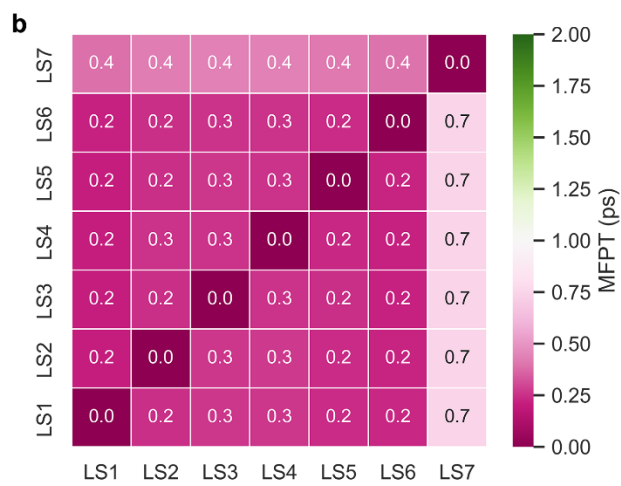
Supplementary Figure 14. Projected discrete lithium trajectories from 3D space in one LCS of LPSCI-III (LCS includes lithium vacancies). The initial lithium states are denoted with stars in LCS. The center (edge) represents all (separated) lithium diffusion paths in this LCS, and lithium states (LS) are classified with different colors. The initial position of the lithium atom is denoted with star and the trajectories in 3D space are coloured pink.



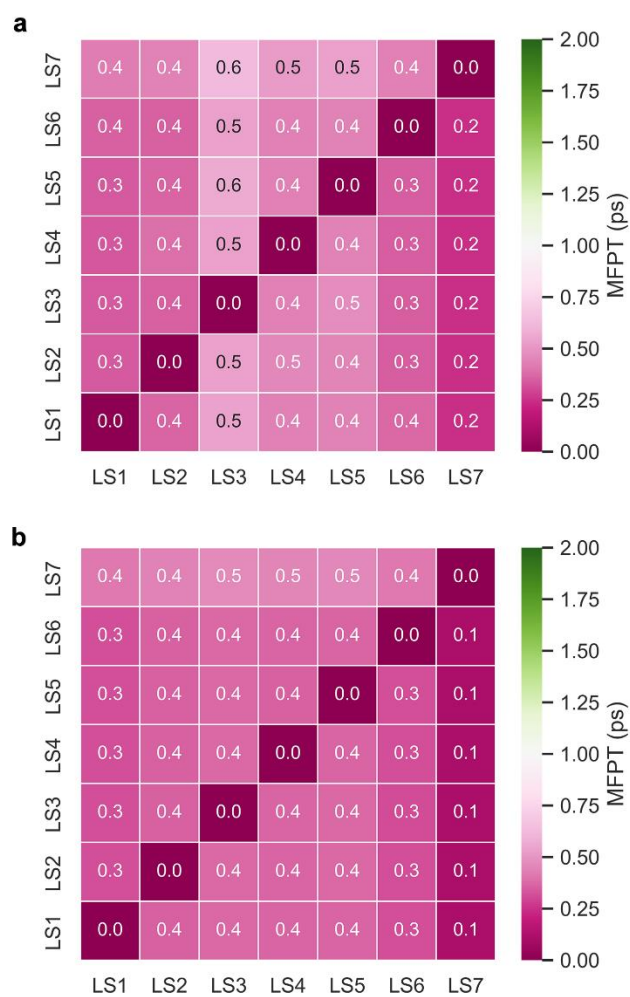
Supplementary Figure 15. Projected discrete lithium trajectories from 3D space in one LCS of LSPSCI. The initial lithium states are denoted with stars in LCS. The center (edge) represents all (separated) lithium diffusion paths in this LCS, and lithium states (LS) are classified with different colors. The initial position of the lithium atom is denoted with star and the trajectories in 3D space are coloured pink.



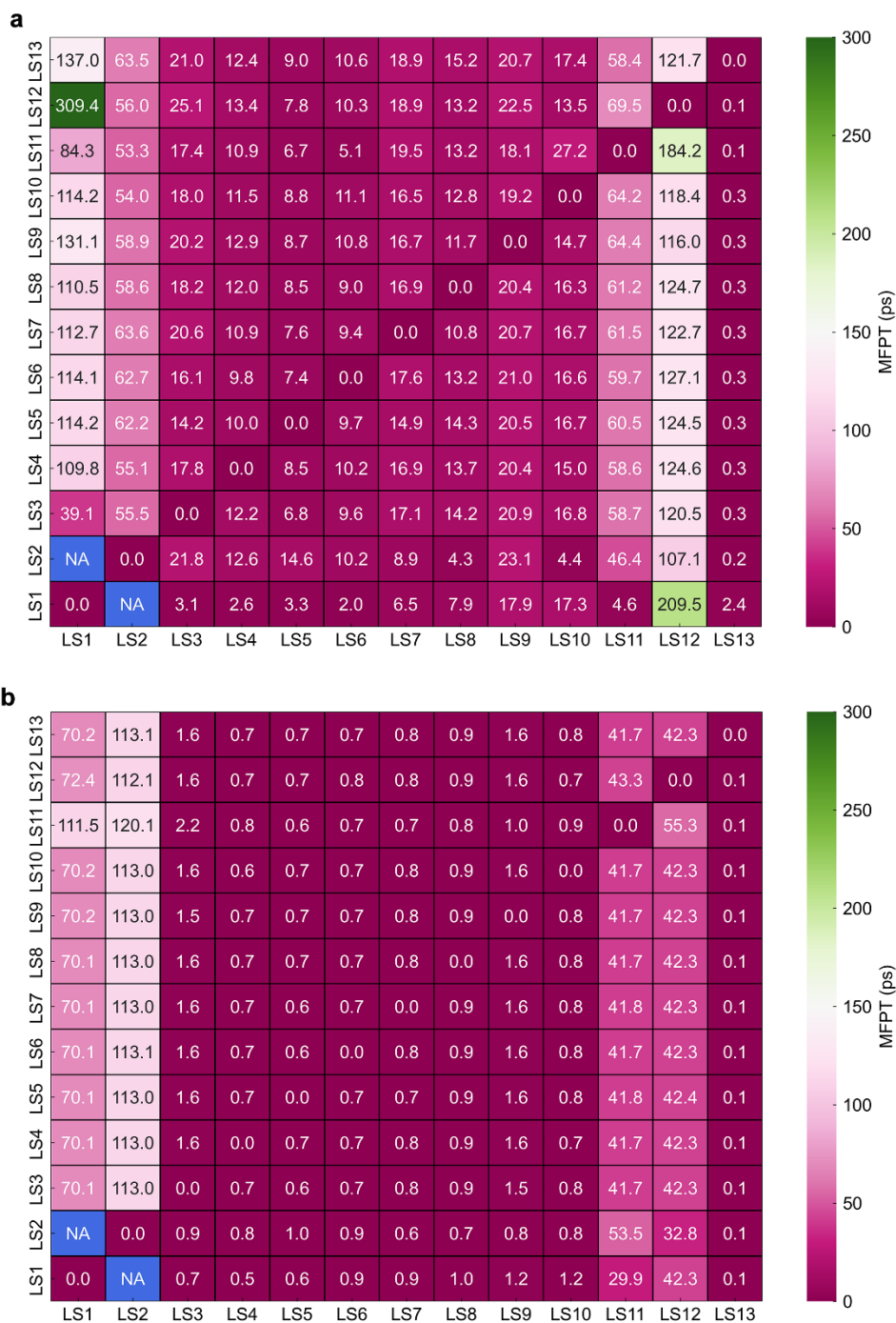
Supplementary Figure 16. MFPT heatmap of lithium hopping in LSPSCl at 300 K.



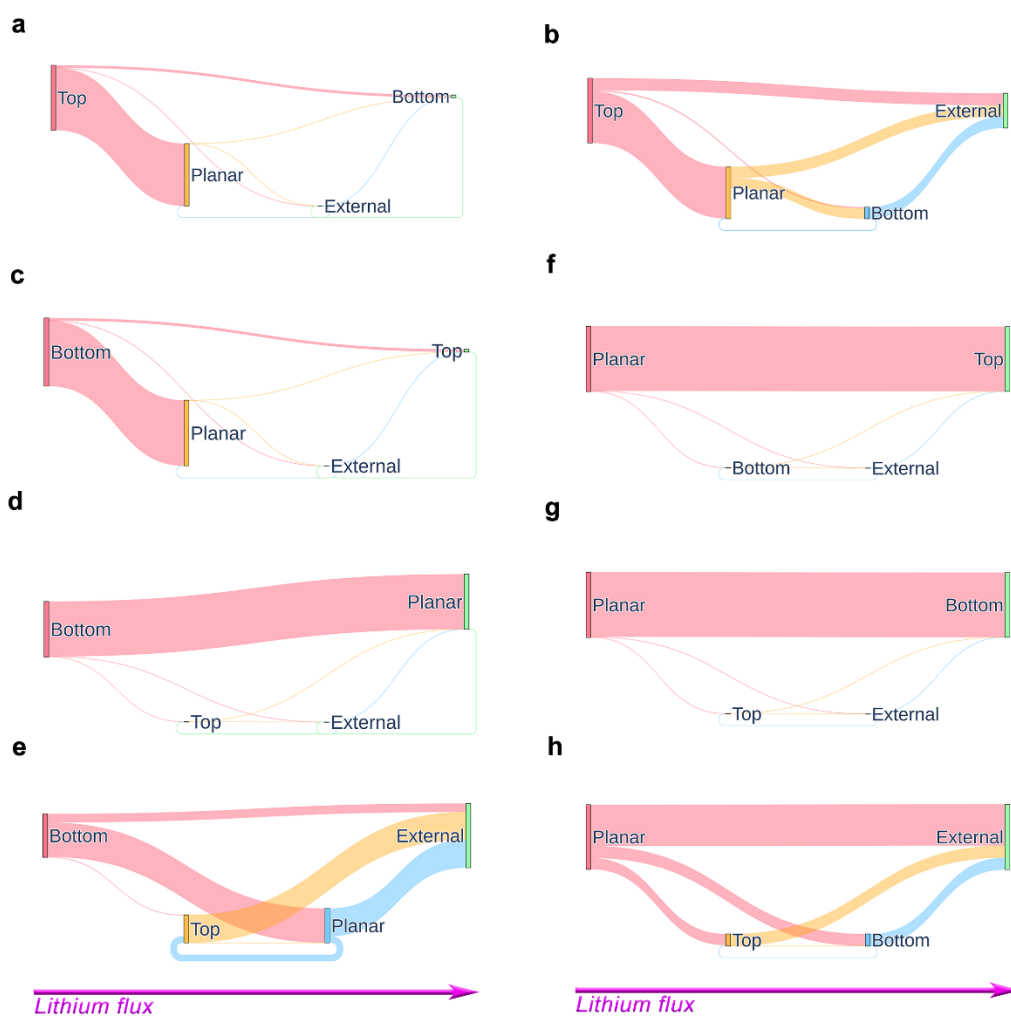
Supplementary Figure 17. MFPT heatmap of LPSCI-II at **a**, 600 K and **b**, 900 K, respectively.



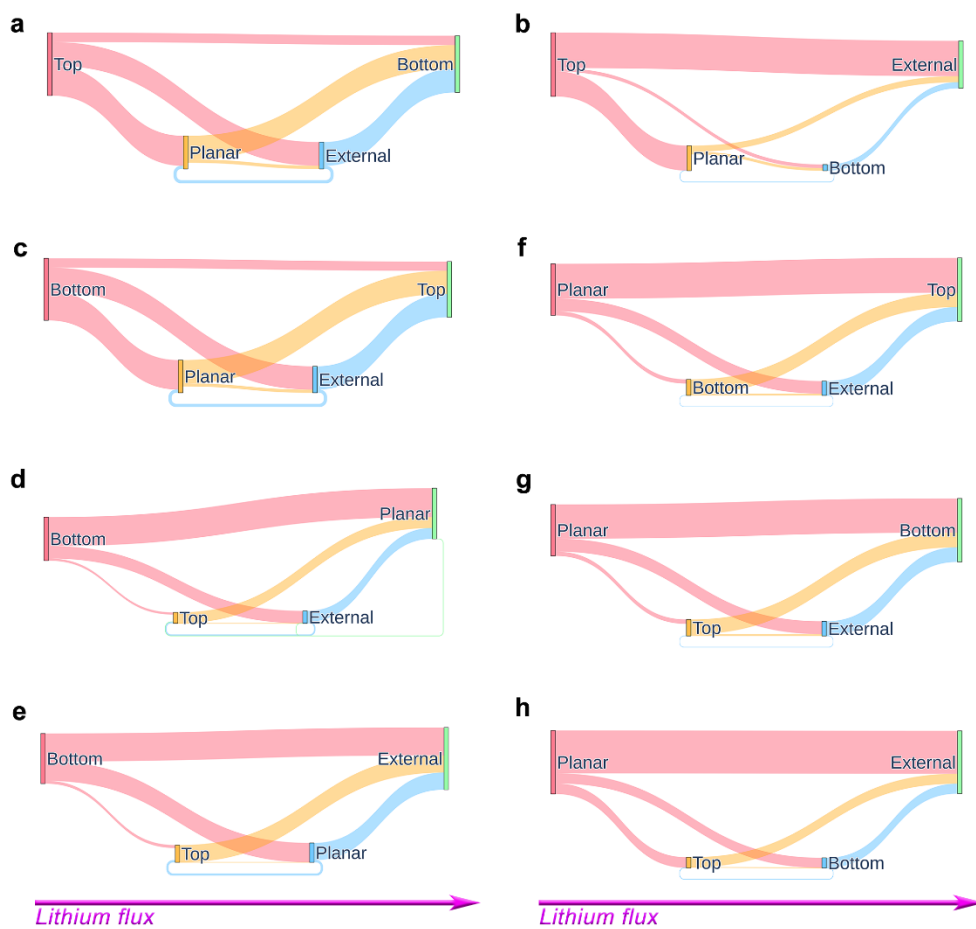
Supplementary Figure 18. MFPT heatmap of LPSCl-III at **a**, 600 K and **b**, 900 K, respectively.



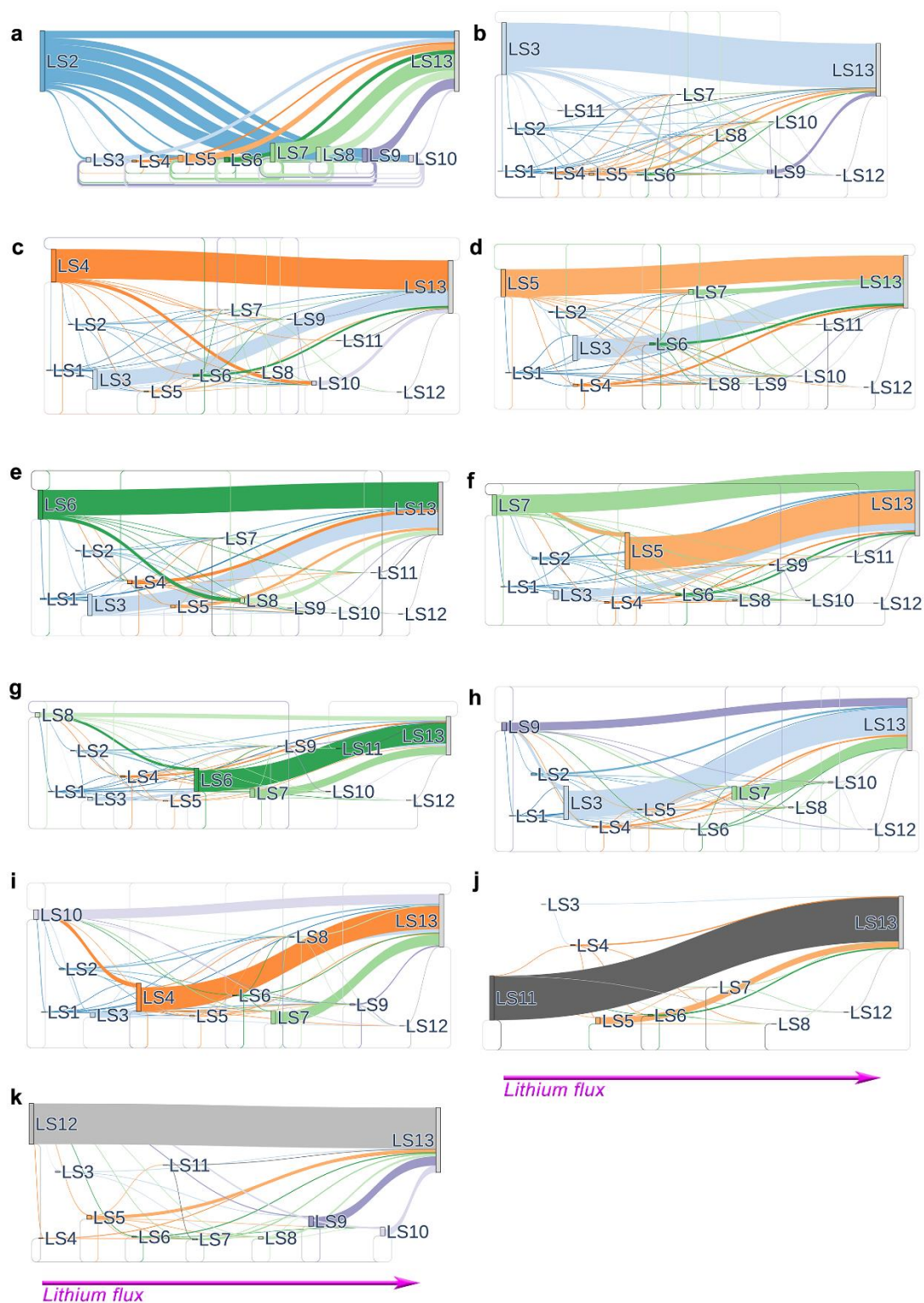
Supplementary Figure 19. MFPT heatmap of LSPSCl at **a**, 600 K and **b**, 900 K, respectively.

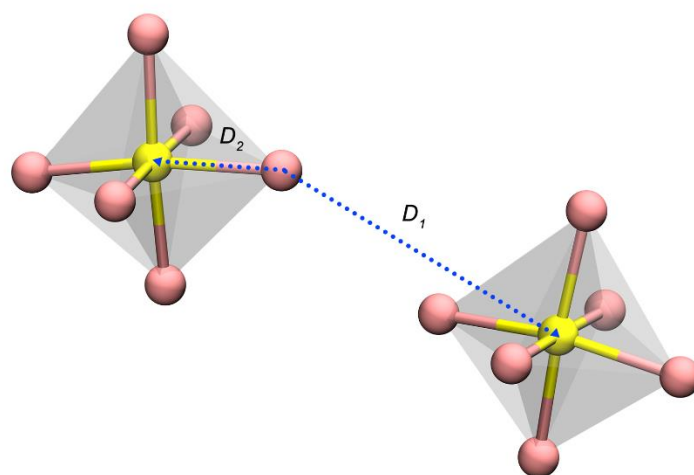


Supplementary Figure 20. Lithium flux in LCSs of LPSCI-II. a, from top to planar, b, from top to external, c, from bottom to top, d, from bottom to planar, e, from bottom to external the LCS, f, from planar to top, g, from planar to bottom, and h, from planar to external the LCS.

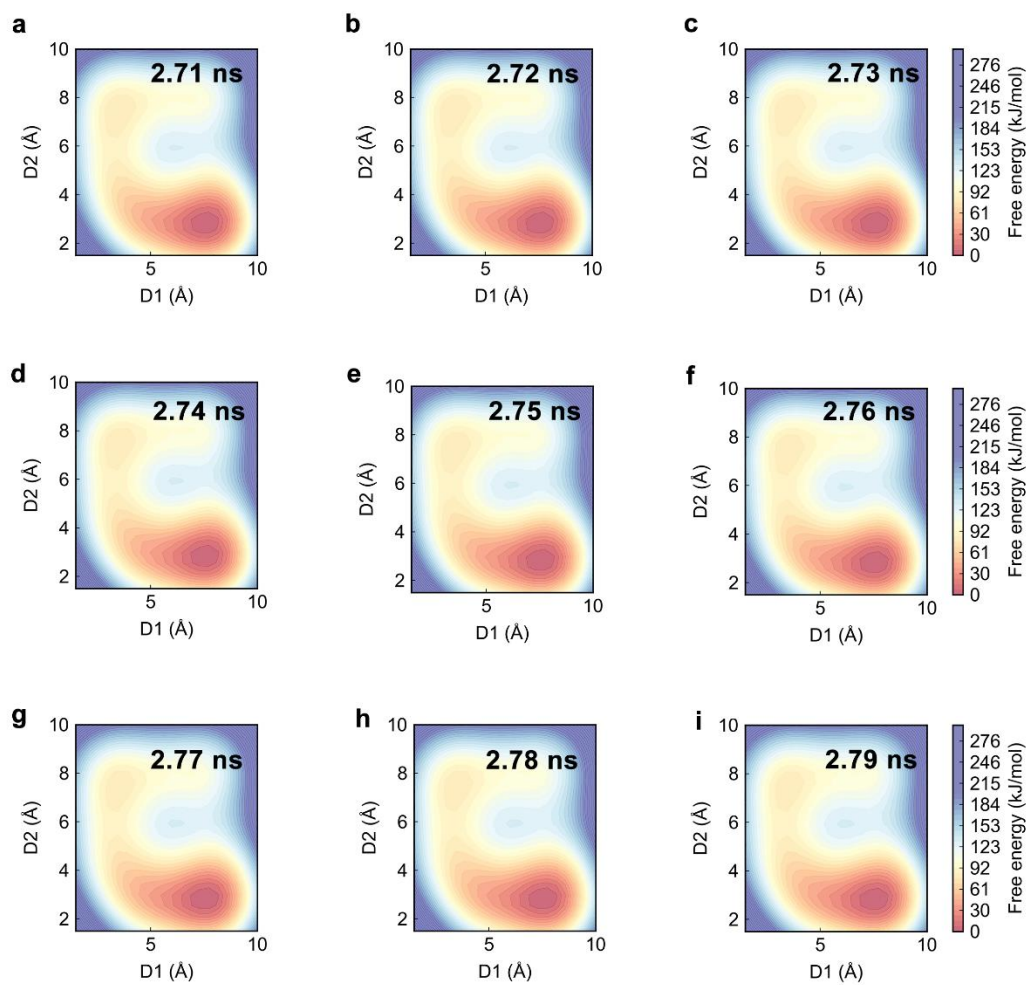


Supplementary Figure 21. Lithium flux in LCSs of LPSCI-III. **a**, from top to planar, **b**, from top to external, **c**, from bottom to top, **d**, from bottom to planar, **e**, from bottom to external the LCS, **f**, from planar to top, **g**, from planar to bottom, and **h**, from planar to external the LCS.

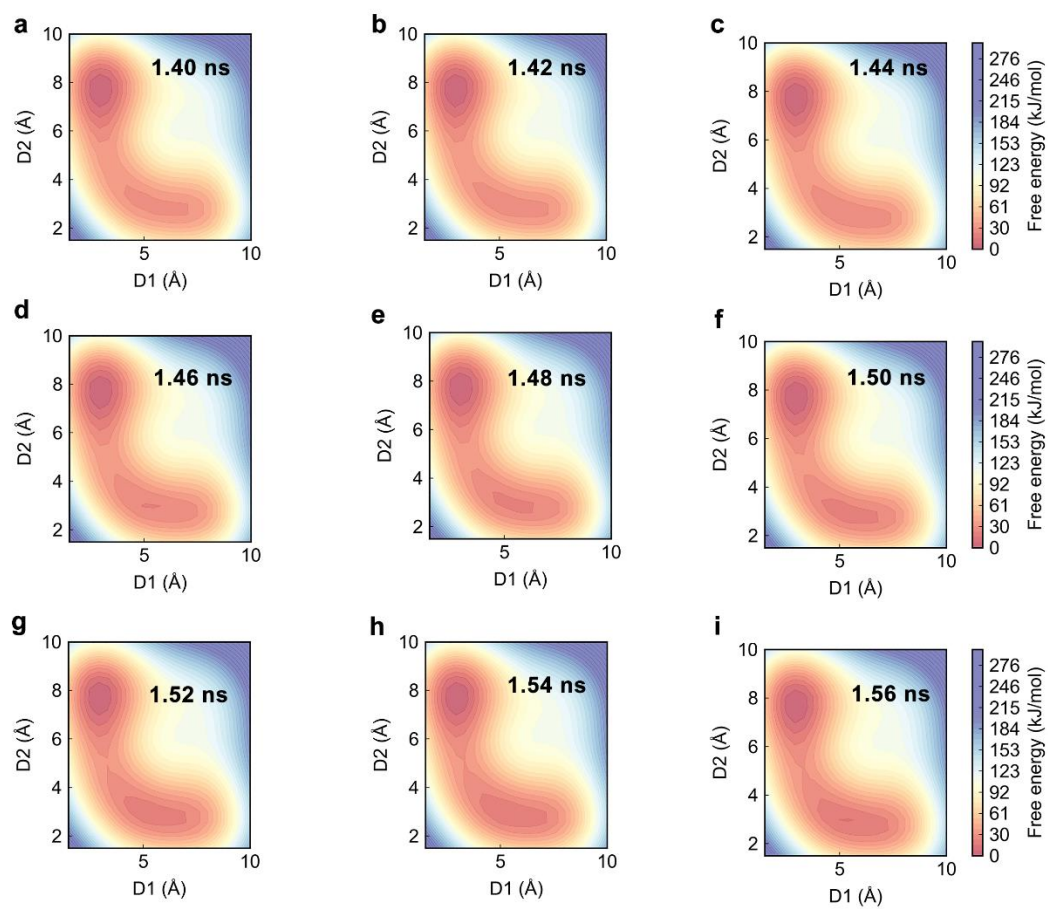




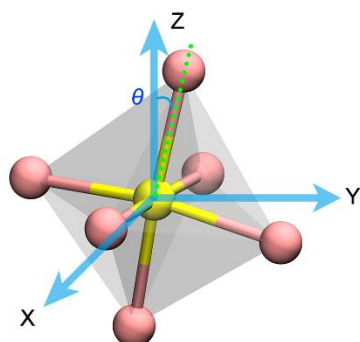
Supplementary Figure 23. Definition of the D_1 and D_2 in LPSCl-II and LPSCl-III.



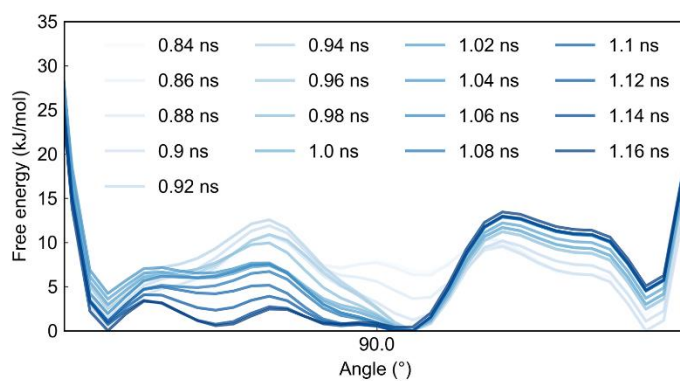
Supplementary Figure 24. Free energy convergence plot of intra-cage lithium diffusion of LPSC1-II from 2.71 ns to 2.79 ns.



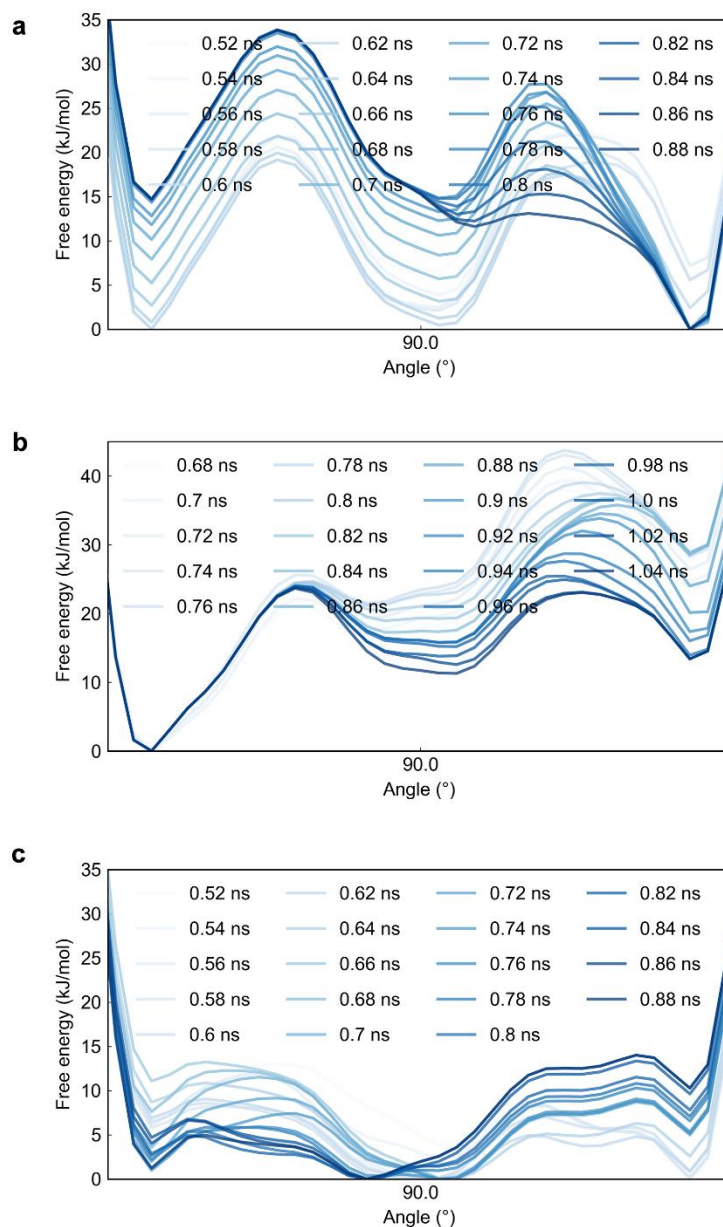
Supplementary Figure 25. Free energy convergence plot of intra-cage lithium diffusion of LPSC1-III from 1.40 ns to 1.56 ns.



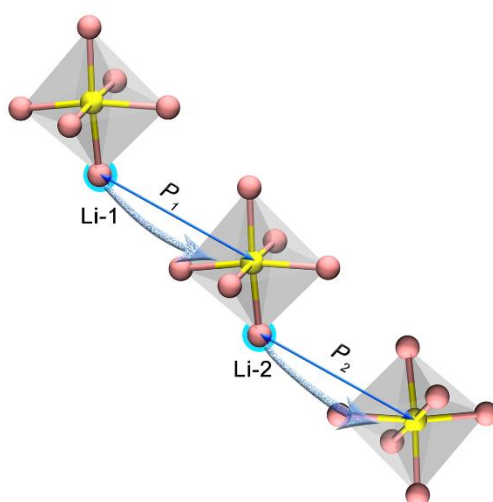
Supplementary Figure 26. Definition of the rotation angle θ in LPSCl-II and LPSCl-III.



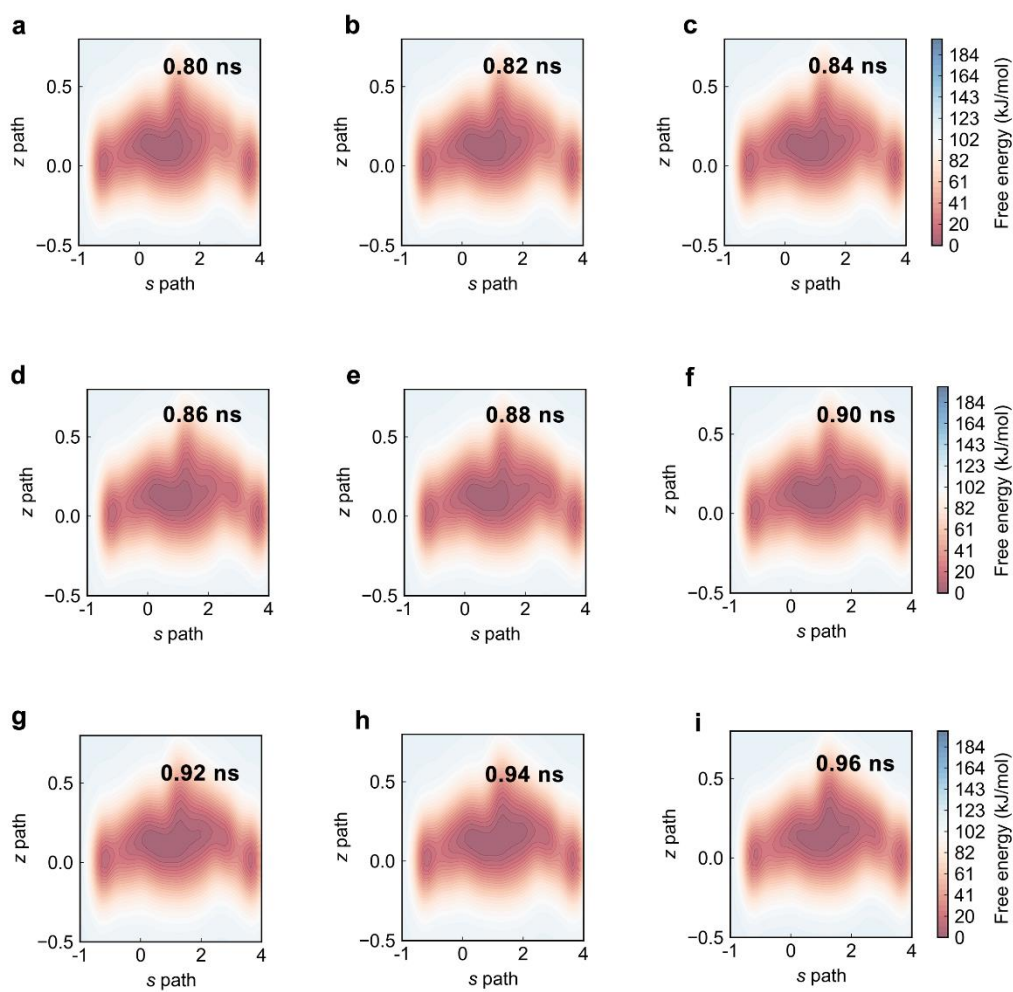
Supplementary Figure 27. Free energy convergence of inter-cage lithium diffusion in LPSCl-II from 0.84 ns to 1.16 ns.



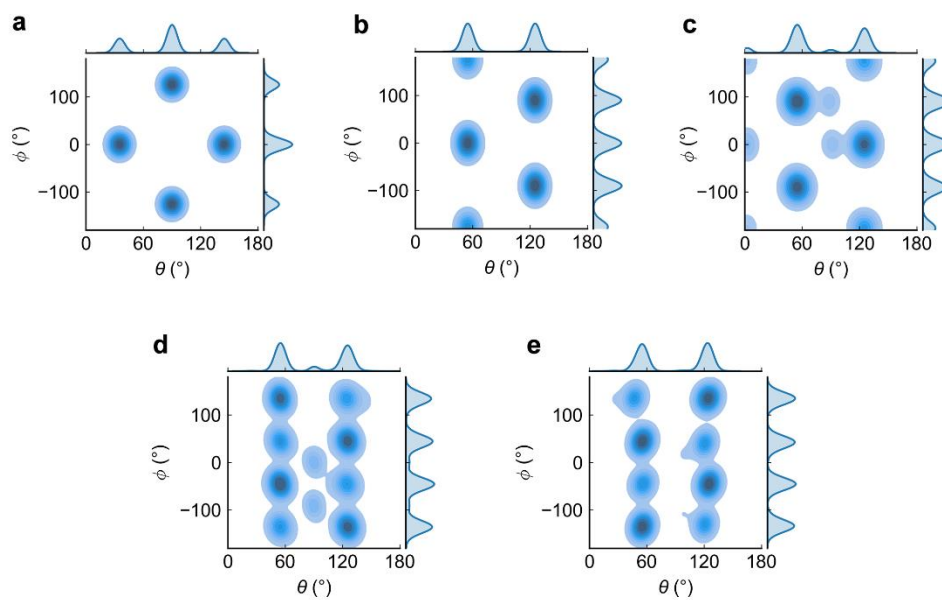
Supplementary Figure 28. Free energy convergence of inter-cage lithium diffusion in LPSCl-III. **a**, Free energy convergence of the inter-cage lithium diffusion in S-centered LCS from 0.52 ns to 0.88 ns. **b**, Free energy convergence of the inter-cage lithium diffusion in Cl-centered LCS from 0.68 ns to 1.04 ns. **c**, Free energy convergence of the inter-cage lithium diffusion in S-centered LCS with one lithium vacancy from 0.52 ns to 0.8 ns.



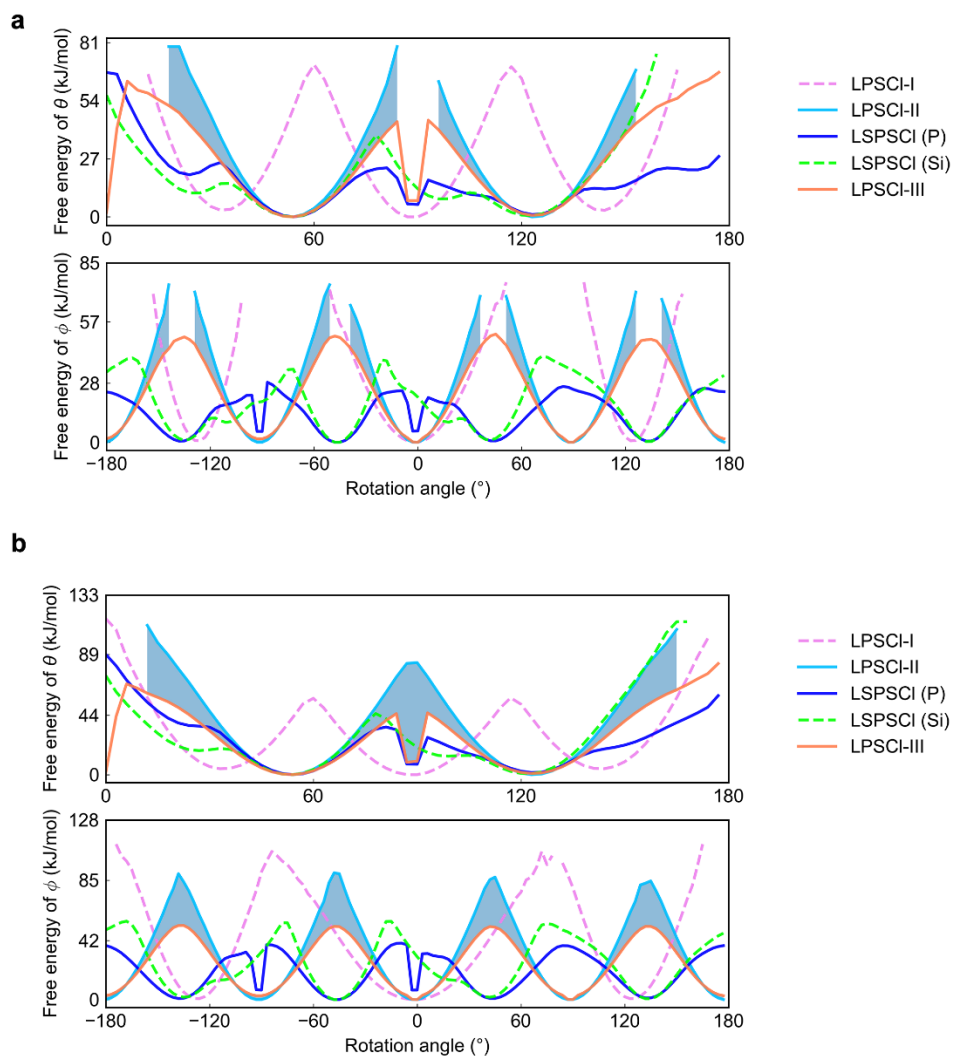
Supplementary Figure 29. Definition of the high dimensional nodes P_1 and P_2 in LPSCI-II and LPSCI-III.



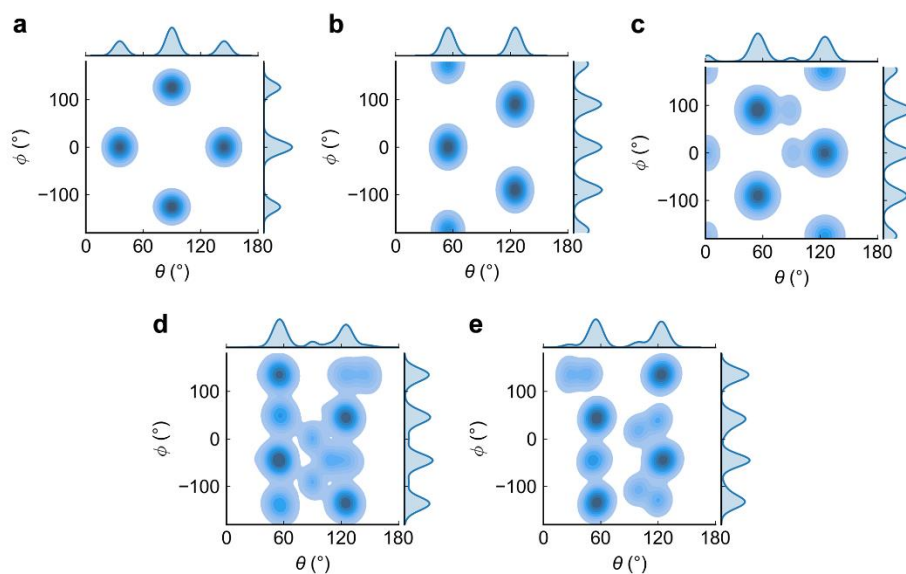
Supplementary Figure 30. Free energy convergence of concerted lithium diffusion in LPSCl-II from 0.80 ns to 0.96 ns.



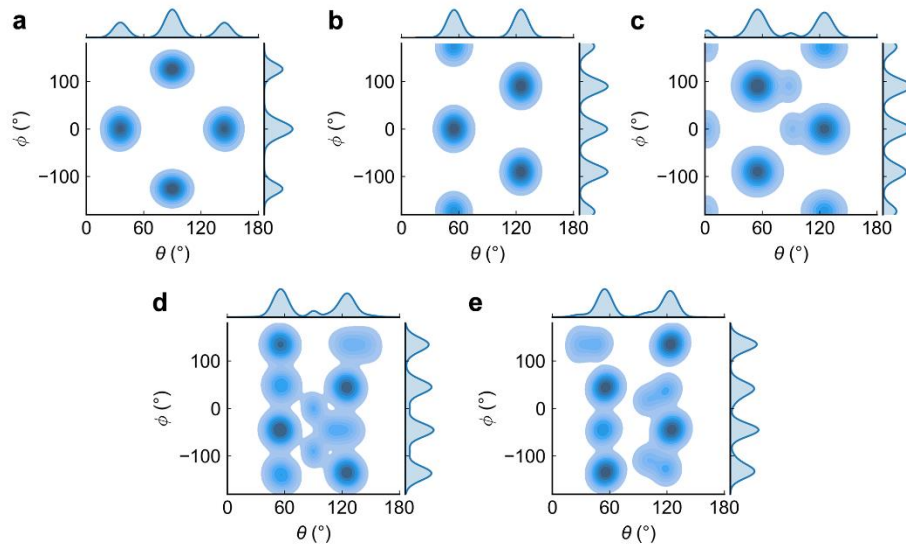
Supplementary Figure 31. Distribution of rotation angles at 300K from **a**, LPSCl-I, **b**, LPSCl-II, **c**, LPSCl-III, **d**, LSPSCl (P centered tetrahedron) and **e**, LSPSCl (Si centered tetrahedron).



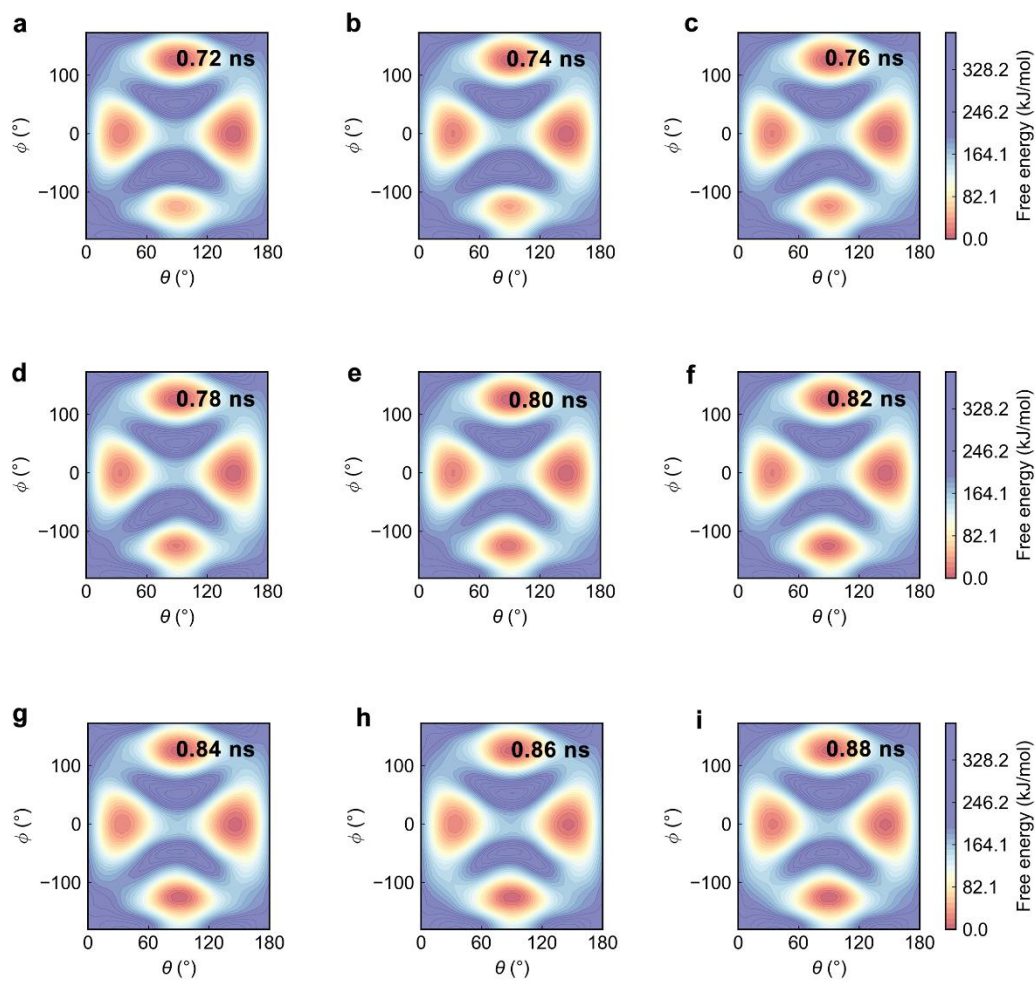
Supplementary Figure 32. Free energy plot of tetrahedral anion framework distortion at **a**, 600 K and **b**, 900K, respectively. The blue shadowed area denoted the free energy difference between LPSCI-II and LPSCI-III.



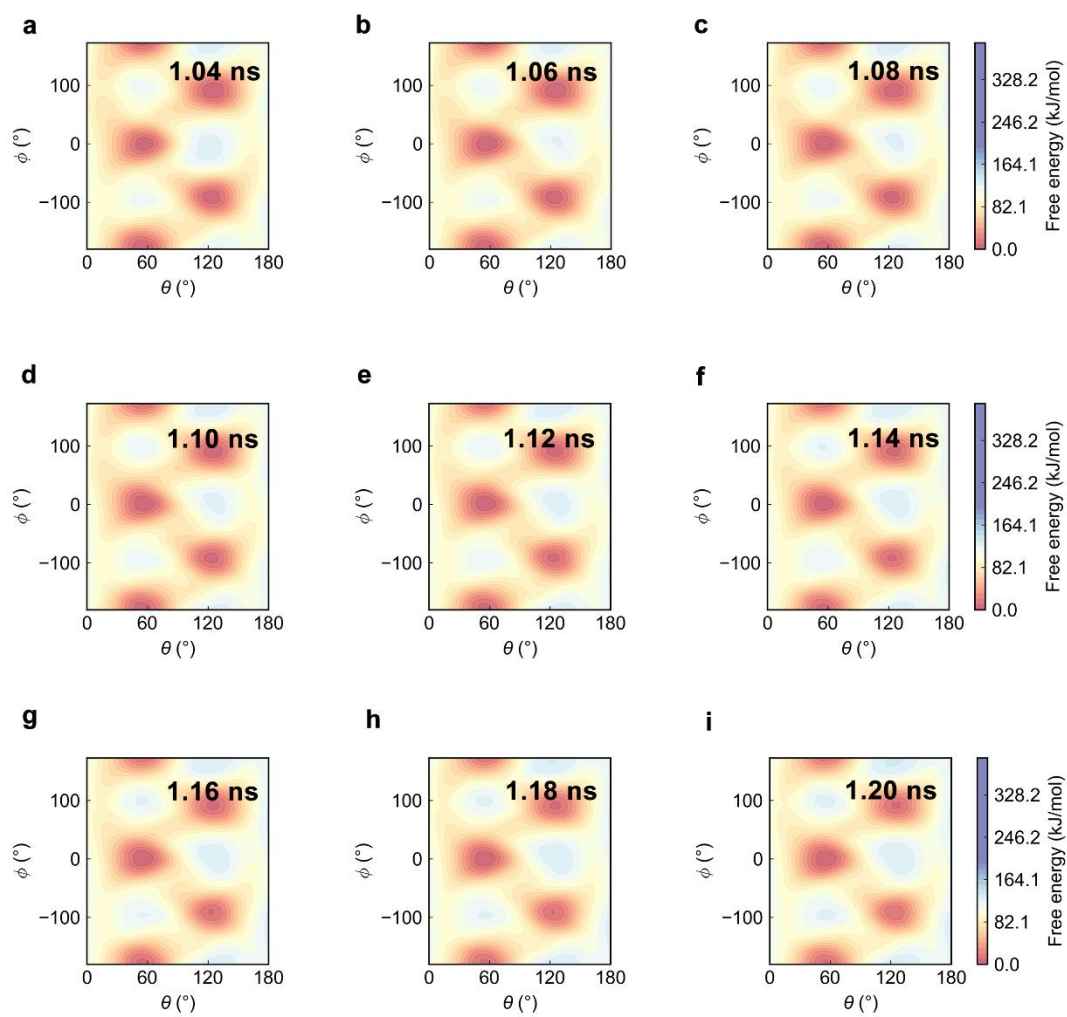
Supplementary Figure 33. Distribution of rotation angles at 600K from **a**, LPSCI-I, **b**, LPSCI-II, **c**, LPSCI-III, **d**, LSPSCI (P centered tetrahedron) and **e**, LSPSCI (Si centered tetrahedron).



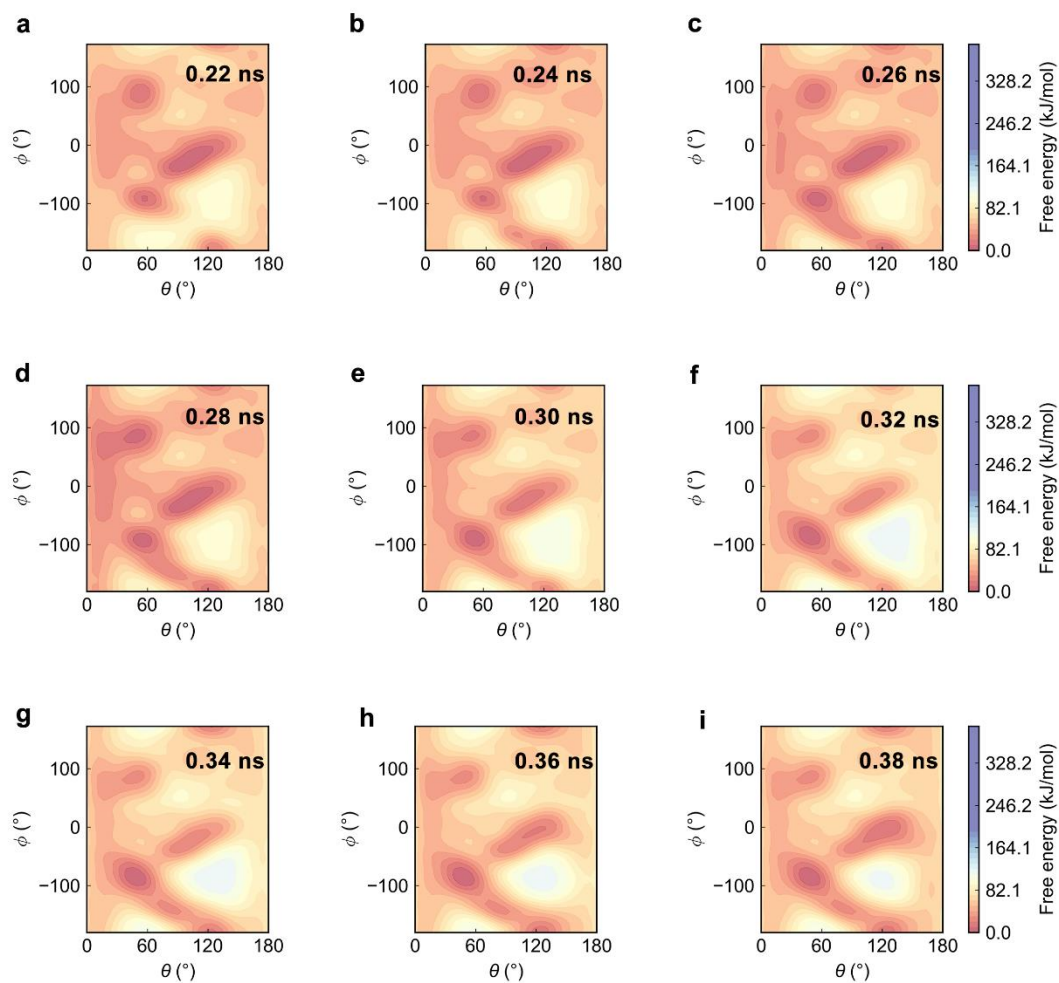
Supplementary Figure 34. Distribution of rotation angles at 900K from **a**, LPSCI-I, **b**, LPSCI-II, **c**, LPSCI-III, **d**, LSPSCI (P centered tetrahedron) and **e**, LSPSCI (Si centered tetrahedron).



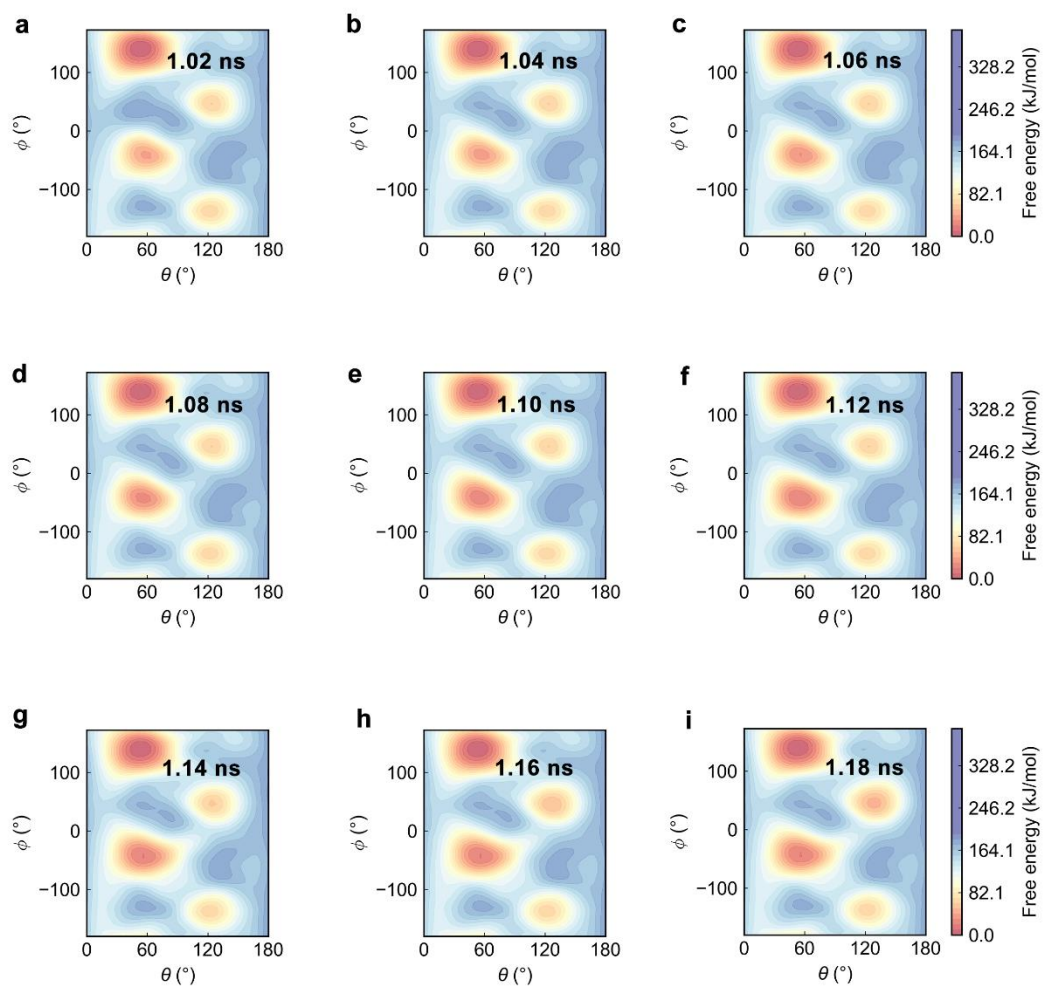
Supplementary Figure 35. Free energy convergence of P-S rotation at 300 K in LPSCI-I from 0.72 ns to 0.88 ns.



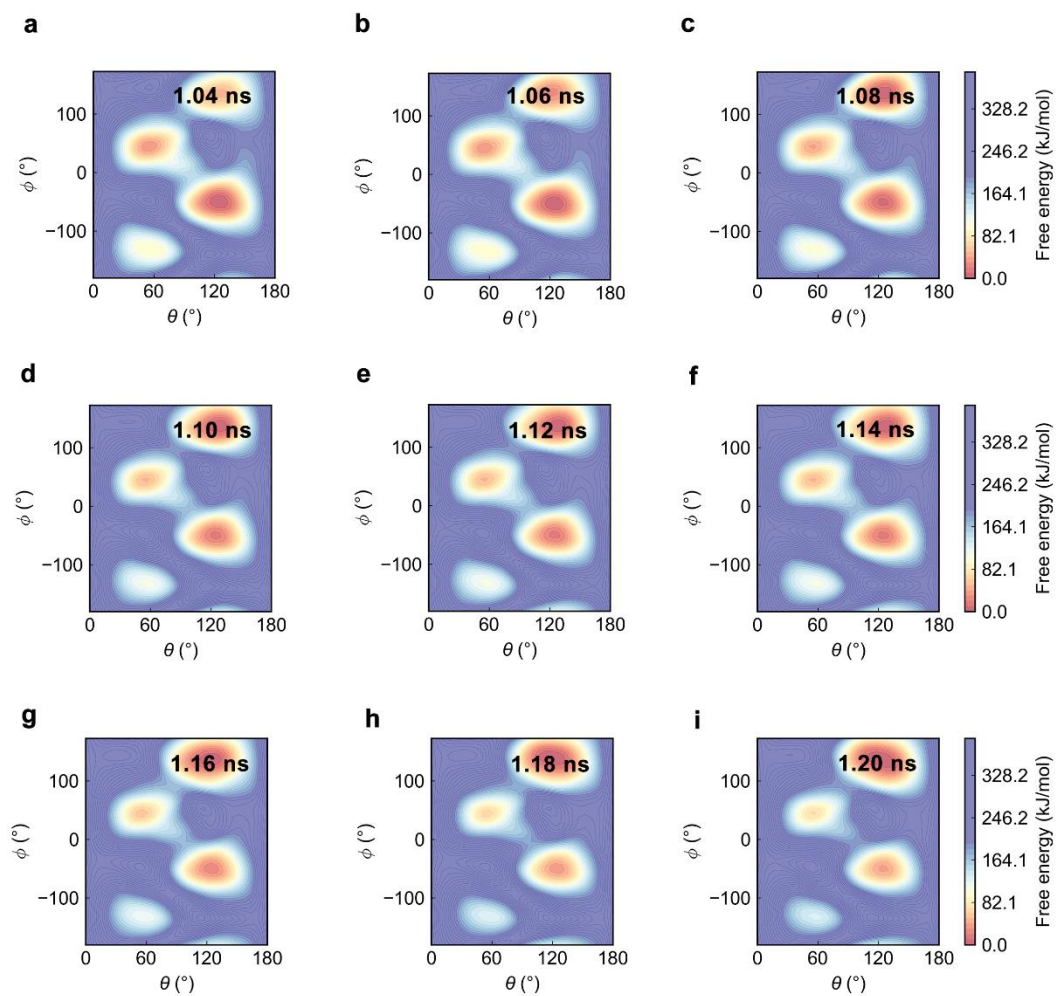
Supplementary Figure 36. Free energy convergence of P-S rotation at 300 K in LPSCI-II from 1.04 ns to 1.20 ns.



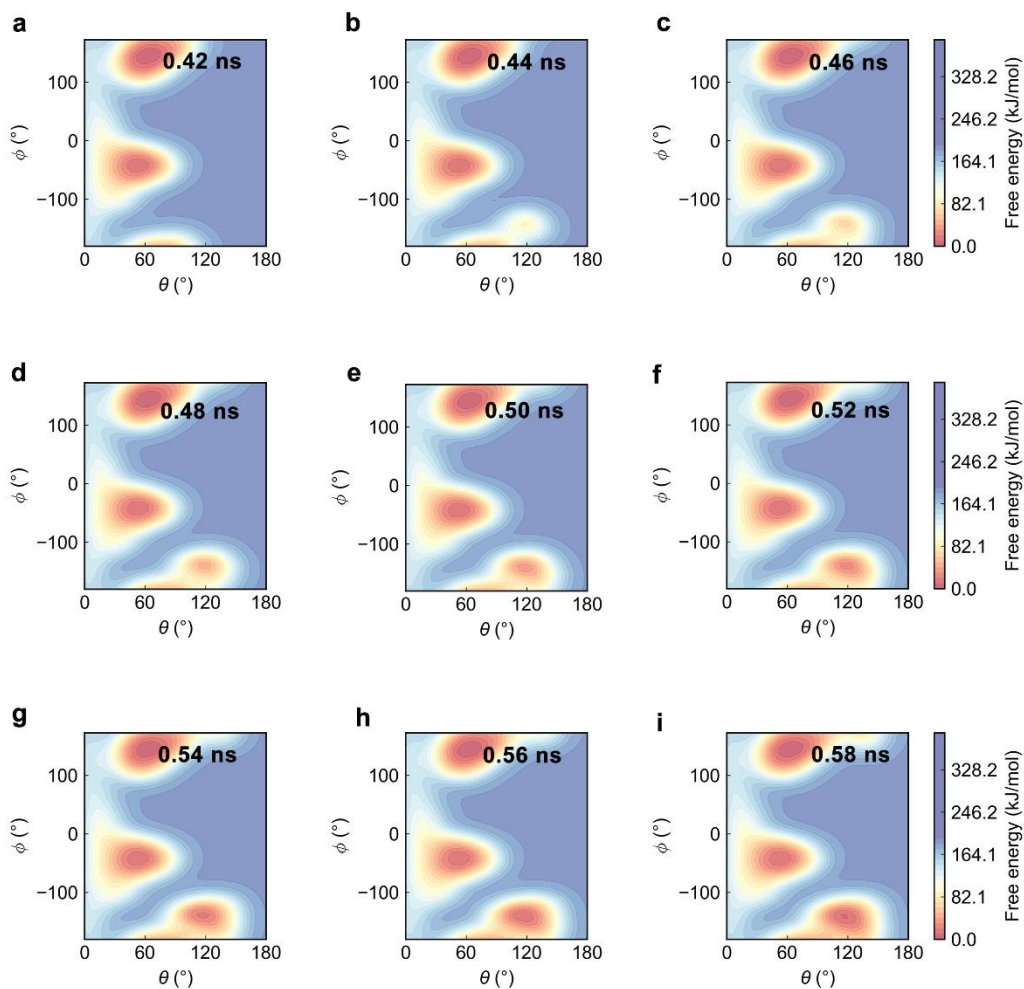
Supplementary Figure 37. Free energy convergence of P-S rotation at 300 K in LPSCI-III from 0.22 ns to 0.38 ns.



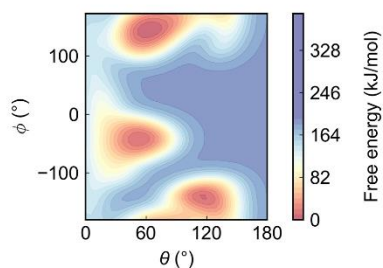
Supplementary Figure 38. Free energy convergence of P-S rotation at 300 K in LSPSCI from 1.02 ns to 1.18 ns.



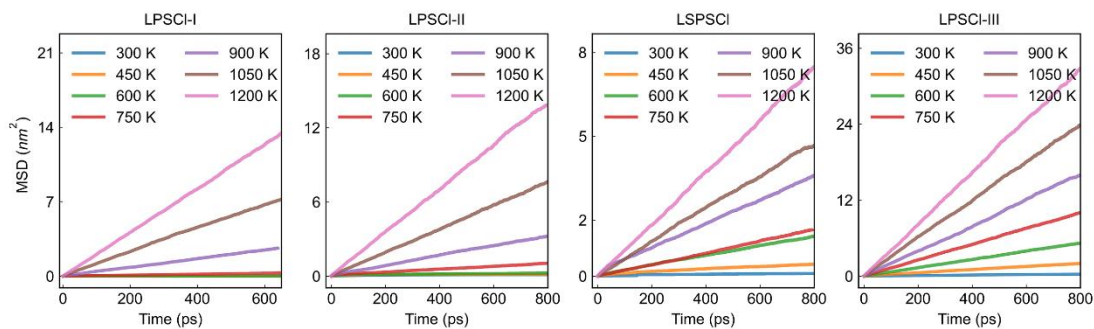
Supplementary Figure 39. Free energy convergence of Si-S rotation at 300 K in LPSCI-I from 1.04 ns to 1.20 ns.



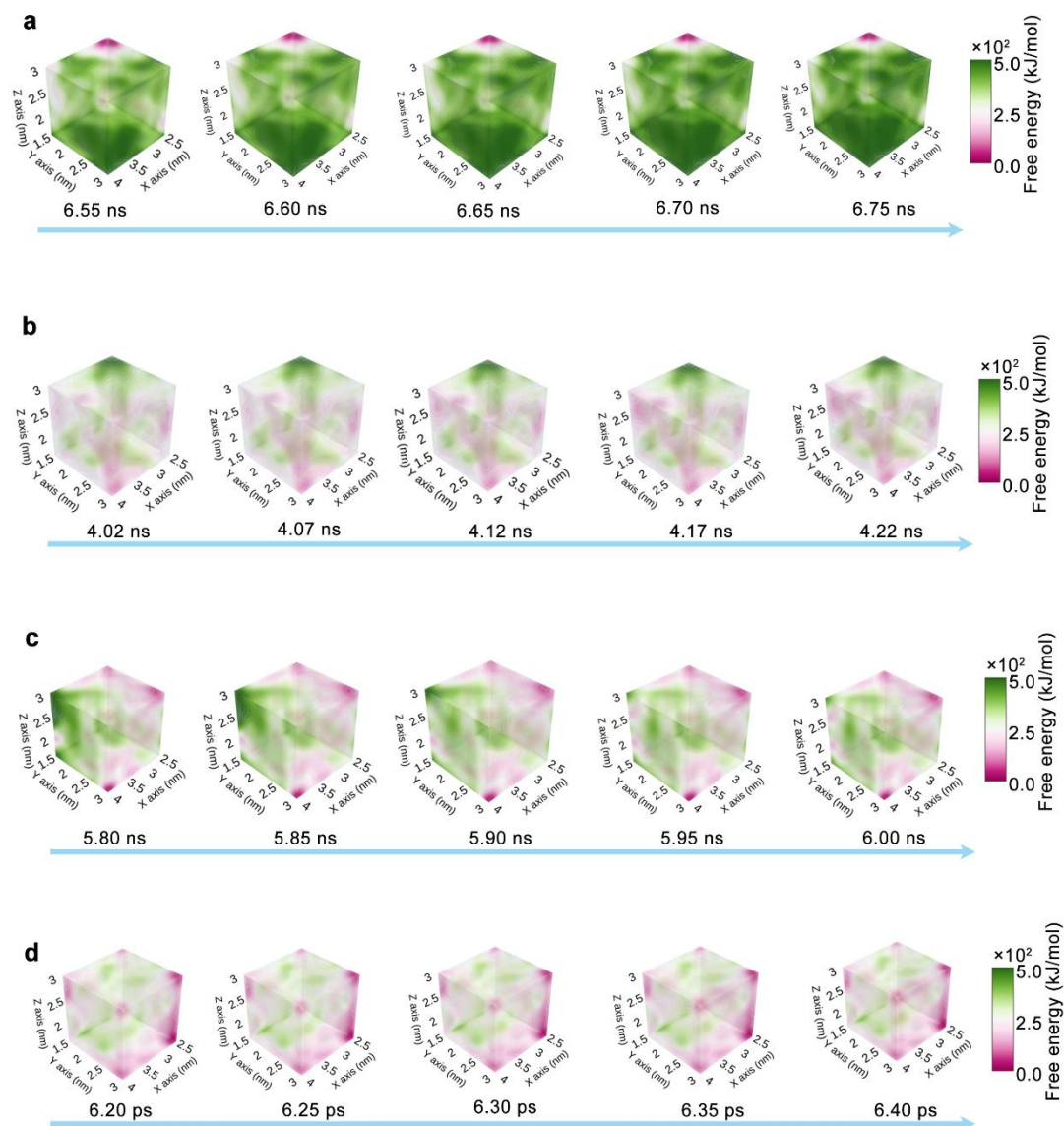
Supplementary Figure 40. Free energy convergence of Si-Cl rotation at 300 K in LSPSCl from 0.42 ns to 0.58 ns.



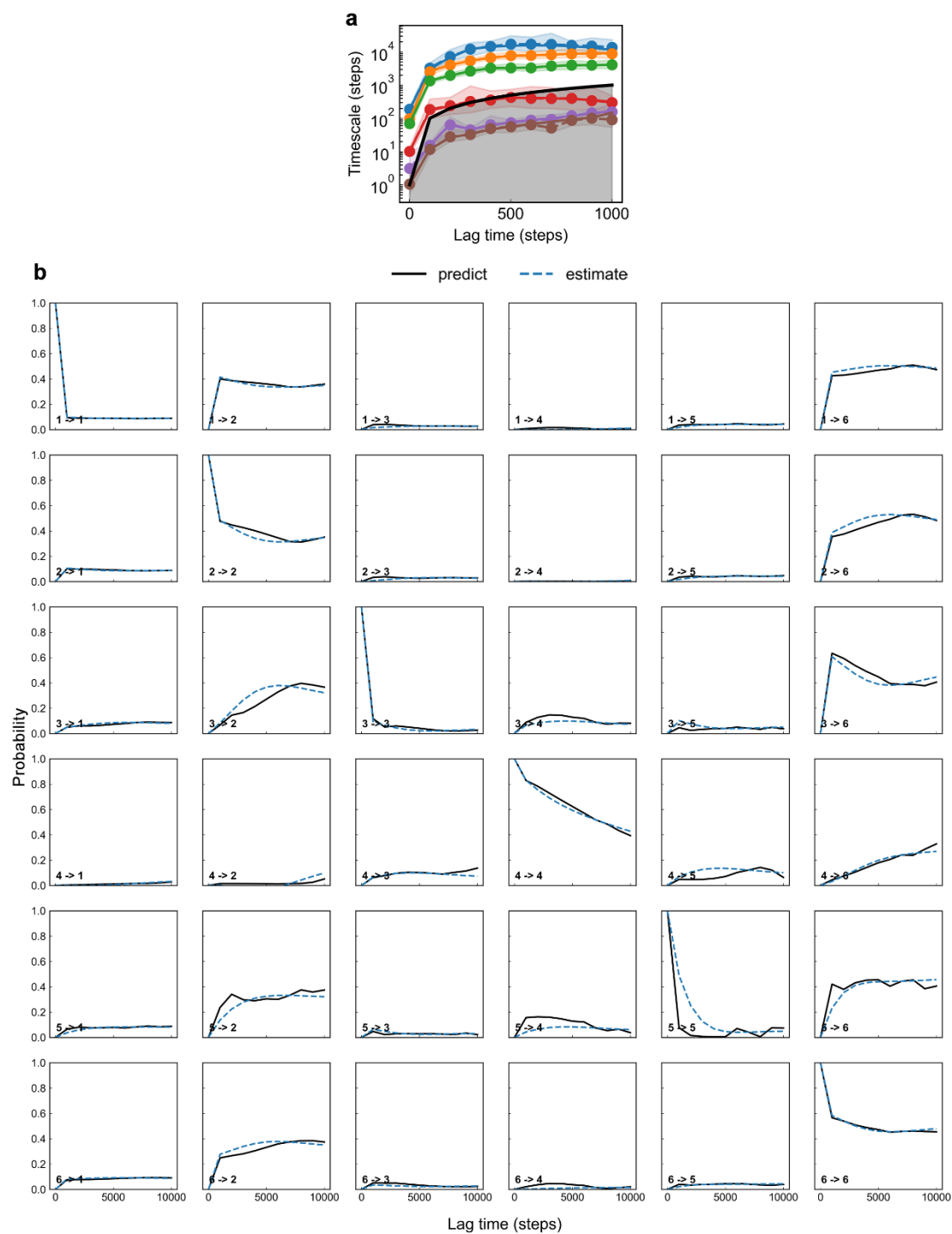
Supplementary Figure 41. The rotation free energy plot of the $[\text{Si}_3\text{Cl}]^-$ units in LSPSCl.



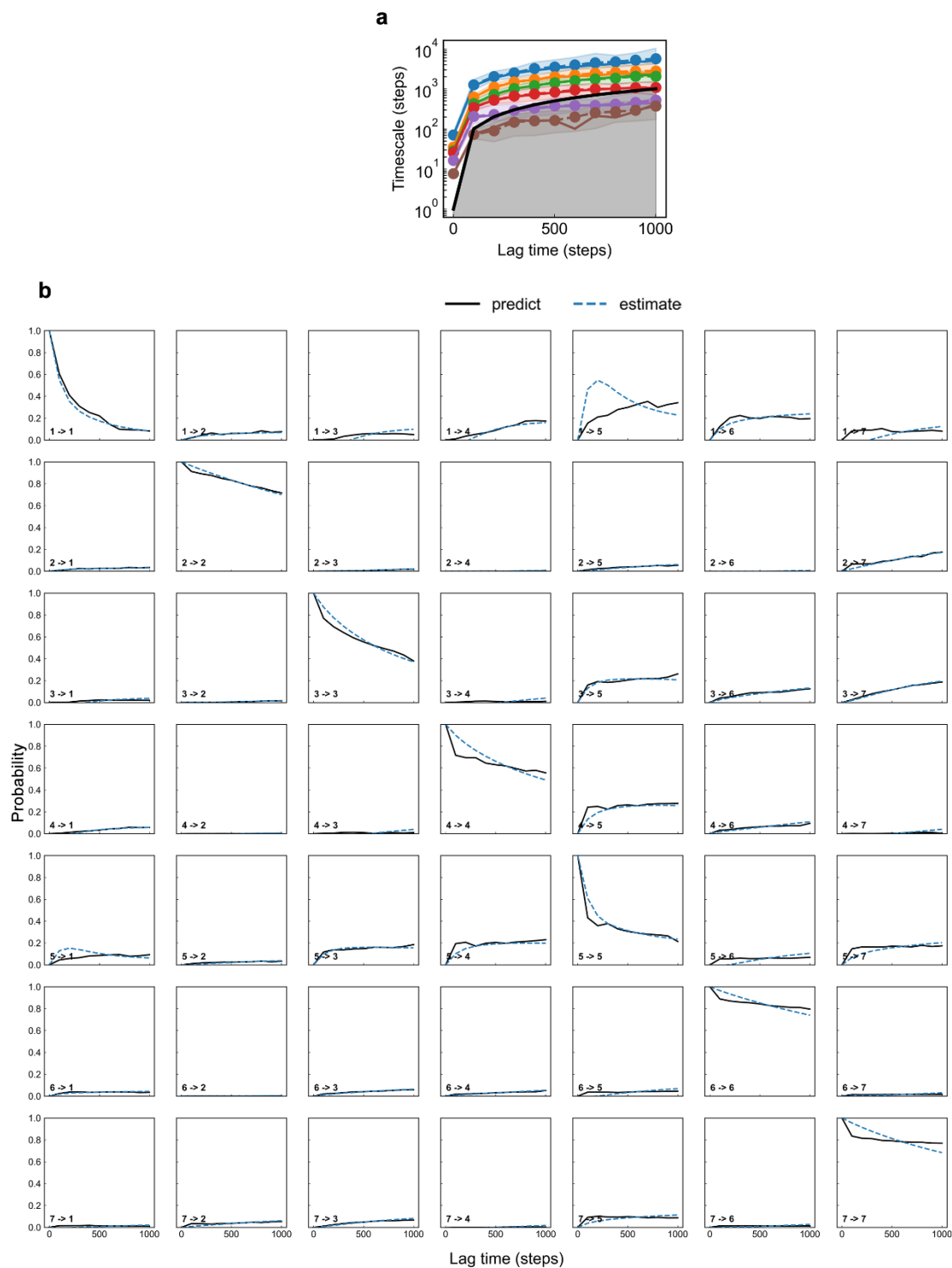
Supplementary Figure 42. Mean squared displacements (MSDs) of all the argyrodite-type SSEs.



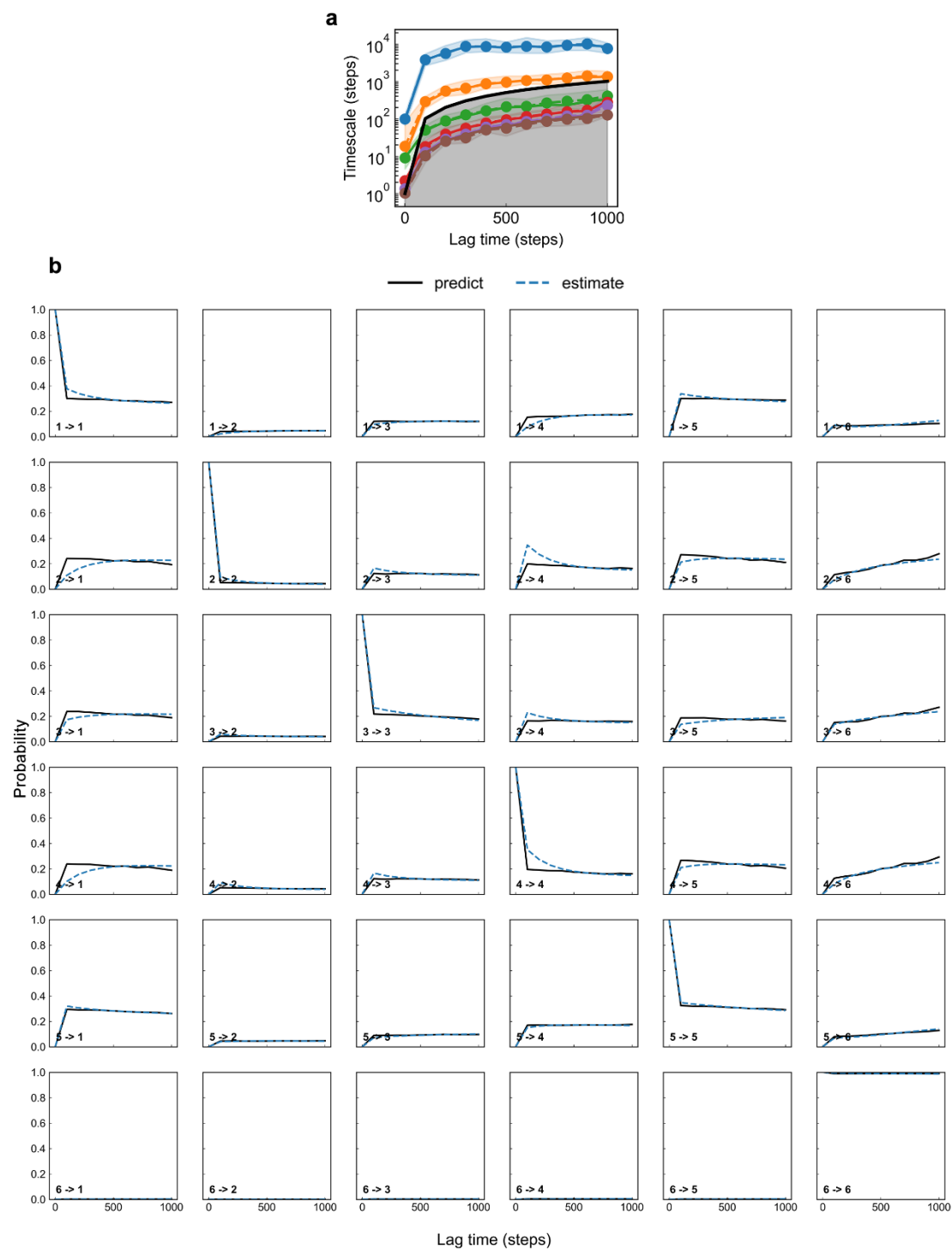
Supplementary Figure 43. 3D free energy convergence at room temperature. **a**, Convergence of LPSCI-I from 6.55 ns to 6.75 ns. **b**, Convergence of LPSCI-II from 4.02 ns to 4.22 ns. **c**, Convergence of LSPSCI from 5.80 ns to 6.00 ns. **d**, Convergence of LPSCI-III from 6.20 ns to 6.40 ns.



Supplementary Figure 44. Chapman-Kolmogorov test for all the populated Lithium states in LCS of LPSCI-II. **a**, Implied timescales (or ITS) for the ten slowest dynamic modes as a function of lag time. **b**, Chapman-Kolmogorov test for the 6 most populated microstates.



Supplementary Figure 45. Chapman-Kolmogorov test for all the populated Lithium states in LCS of LPSCl-III. **a**, Implied timescales (or ITS) for the ten slowest dynamic modes as a function of lag time. **b**, Chapman-Kolmogorov test for the 7 most populated microstates.



Supplementary Figure 46. Chapman-Kolmogorov test for all the populated Lithium states in LCS of LSPSCI. **a**, Implied timescales (or ITS) for the ten slowest dynamic modes as a function of lag time. **b**, Chapman-Kolmogorov test for the 6 most populated microstates.

Supplementary Table 1. The parameters for training the NNPs.

SSE type	Cutoff (Å)	Hidden layers	Fitting layers	Learning rate	Decay rate	Energy pre-factor	Force pre-factor
LPSCI-II	8.5	25, 50, 100	240, 240, 240	0.001	2000	0.02	1000
LPSCI-I	8.5	25, 50, 100	240, 240, 240	0.001	2000	0.02	1000
LSPSCI	6.5	25, 50, 100	480, 480, 480	0.001	2000	0.02	2000
LPSCI-III	6.5	25, 50, 100	480, 480, 480	0.001	2000	0.02	1000

Supplementary Table 2. MAEs of NNPs.

SSE type	LPSCI-I	LPSCI-II	LSPSCI	LPSCI-III
Energy MAE (meV/atom)	1.11 ± 0.02	1.15 ± 0.03	0.96 ± 0.02	0.58 ± 0.02
Force MAE (meV/Å)	38.15 ± 0.35	27.47 ± 0.08	42.27 ± 0.34	37.07 ± 0.66

Supplementary Table 3. Path entropy S_p in LCSs of LPSCI-II and LPSCI-III.

Flux pattern/SSE	LPSCI-II	LPSCI-III
Top \rightarrow Bottom	0.15	1.35
Top \rightarrow Plane	0.052	0.78
Top \rightarrow External	0.85	0.90
Bottom \rightarrow Top	0.15	1.35
Bottom \rightarrow Plane	0.053	0.81
Bottom \rightarrow External	0.84	0.91
Plane \rightarrow Top	0.052	0.84
Plane \rightarrow Bottom	0.052	0.86
Plane \rightarrow External	0.79	0.77

Supplementary Table 4. Path entropy S_p in LCSs of LSPSCI.

Flux pattern/SSE	LSPSCI
LS1 \rightarrow LS2	0.00
LS1 \rightarrow LS3	0.19
LS1 \rightarrow LS4	0.16
LS1 \rightarrow LS5	0.27
LS1 \rightarrow LS6	0.049
LS1 \rightarrow LS7	0.014
LS1 \rightarrow LS8	0.042
LS1 \rightarrow LS9	0.50
LS1 \rightarrow LS10	0.69
LS1 \rightarrow LS11	0.00
LS1 \rightarrow LS12	0.00
LS1 \rightarrow LS13	2.99

Supplementary Table 5. The WTmetaD parameters of free energy calculation of distortion in tetrahedron units.

SSE type	Distortion unit	Deposition rate (fs)	Gaussian width	Gaussian height (kJ/mol)	Bias factor
LPSCI-I	[PS ₄] ³⁻	50	0.25	5	20
LPSCI-II	[PS ₄] ³⁻	100	0.25	2	10
LPSCI-III	[PS ₄] ³⁻	100	0.25	2	20
LSPSCI	[PS ₄] ³⁻	100	0.25	2	20
LSPSCI	[SiS ₄] ⁴⁻	50	0.25	2	100
LSPSCI	[SiS ₃ Cl] ³⁻	100	0.25	2	20

Supplementary Table 6. The classification parameters and accuracies from SVM.

SSE type	Cutoff (nm)	Regularization parameter C	Number of radial functions	Training accuracy	Testing accuracy
LPSCI-I	0.6	200	37	0.98	0.99
LPSCI-II	0.6	200	37	0.79	0.77
LPSCI-III	0.6	200	37	0.58	0.57
LSPSCI	0.6	200	37	0.64	0.60

Supplementary Table 7. The classification parameters and accuracies from logistic regression.

SSE type	Cutoff (nm)	Number of layers	Number of radial functions	Training accuracy	Testing accuracy
LPSCI-I	0.6	2	37	0.99	0.98
LPSCI-II	0.6	2	37	0.83	0.86
LPSCI-III	0.6	2	37	0.72	0.73
LSPSCI	0.6	2	37	0.76	0.75

1. Supplementary Note 1

Neural-network interatomic potential validation and accuracy.

To validate the NNPs, the mean absolute errors (MAEs) of all the models are listed in **Supplementary Table 2**. We also plot the comparison between the energy calculated from DFT and predicted from our trained models. (**Supplementary Figures 5 to 8**) In addition, the radial distribution functions (RDFs) of lithium are calculated and compared between the results from DFT and NNP predictions. (**Supplementary Figure 9**) From these assessments, the trained models are ready to use in the following production.

2. Supplementary Note 2

Details of WTmetaD simulations.

2.1. Inter-cage diffusion

For lithium diffusion across the LCSs, the collective variables are defined as two distances from the neighboring coordination center. (**Supplementary Figure 23**) The simulation parameters setup for WTmetaD employs Gaussian “hills” with a deposition rate of 100 fs, width of 0.20 Å, bias factor of 20, and height of 5.0 kJ/mol for LPSCI-III. For LPSCI-II, the deposition rate is set to 50 fs, while other parameters remain unchanged. A pair of walls is applied to limit the D_1 and D_2 between 1.5 Å and 8.5 Å to constrain the lithium diffusion in neighboring LCSs.

2.2. Intra-cage diffusion

For the intra-cage diffusion of lithium atom in LPSCI-II and LPSCI-III, the CV is designed as the polar angle formed between bond of lithium and the coordinated center atom (sulfur, chlorine) of LCS with unit vector along Z direction (**Supplementary Figure 26**) as

$$\theta = \cos^{-1} \left(\frac{v_1 \cdot n}{|v_1| |n|} \right) \quad (3)$$

where v_1 is the vector of the Li-S (Cl) bond, and n is the unit vector (0, 0, 1) of the Z axis. The simulation parameters setup for WTmetaD employs Gaussian “hills” with a deposition rate of 100 fs, width of 0.20 Å, bias factor of 10, and height of 2.0 kJ/mol.

A pair of walls is applied to limit the $|v_1|$ between 1.5 Å and 3.0 Å to constrain the lithium stays in LCS.

2.3. The concerted diffusion

To analyze the possible synergy diffusion of lithium in neighboring LCS of LPSCl-II, we use path CV to grab the possible synergy effects.^{16,17} From the defined path CV of two lithium ions, the synergy diffusion is computed from the high-dimensional path. The defined path \mathbf{s} and the distance from the right path \mathbf{s} is \mathbf{z} :¹⁷

$$\mathbf{s} = \mathbf{i}_2 + \text{sign}(\mathbf{i}_2 - \mathbf{i}_1) \frac{\sqrt{(\mathbf{v}_1 \cdot \mathbf{v}_2)^2 - |\mathbf{v}_3|^2 (|\mathbf{v}_1|^2 - |\mathbf{v}_2|^2)}}{2|\mathbf{v}_3|^2} - \frac{\mathbf{v}_1 \cdot \mathbf{v}_3 - |\mathbf{v}_3|^2}{2|\mathbf{v}_3|^2} \quad (4)$$

$$\mathbf{z} = \sqrt{\left[|\mathbf{v}_1|^2 - |\mathbf{v}_2|^2 \left(\frac{\sqrt{(\mathbf{v}_1 \cdot \mathbf{v}_2)^2 - |\mathbf{v}_3|^2 (|\mathbf{v}_1|^2 - |\mathbf{v}_2|^2)}}{2|\mathbf{v}_3|^2} - \frac{\mathbf{v}_1 \cdot \mathbf{v}_3 - |\mathbf{v}_3|^2}{2|\mathbf{v}_3|^2} \right) \right]^2} \quad (5)$$

Where \mathbf{v}_1 and \mathbf{v}_3 are the vectors connecting the current position to the closet and second closet node of the path, \mathbf{v}_2 is the vector connecting \mathbf{v}_1 and \mathbf{v}_3 . The projections of the closet and second closet node are represented in \mathbf{i}_1 and \mathbf{i}_2 .

For analyzing the concerted diffusion of lithium atoms Li-1 and Li-2 from neighboring LCS, we define the high dimensional path as P_1 and P_2 . (**Supplementary Figure 29**) Four nodes of (P_1, P_2) are selected for this path \mathbf{s} , $\{(6.50, 6.50), (5.0, 5.0), (3.5, 3.5), (2.0, 2.0)\}$. The simulation parameters setup for WTmetaD employs Gaussian “hills” with a deposition rate of 100 fs, width of 0.20 Å, bias factor of 10, and height of 2.0 kJ/mol for LPSCl-III. A pair of walls is applied to limit the P_1 and P_2 between 1.5 Å and 8.5 Å to constrain the concerted diffusion that happens in neighboring LCSs.

2.4. Distortion of tetrahedron units

The distortion of tetrahedron units in all four types of SSEs is explored. To get the exact free energy barrier of the rotation, the azimuthal angles θ and ϕ are selected as the CVs. (**Figure 5**) The detailed simulation parameters are listed in **Supplementary Table 5**.

2.5. 3D free energy surface

To construct the 3D free energy surface of the lithium diffusion, three CVs including the X-axis position (Li_x), Y-axis position (Li_y), and Z-axis position (Li_z) of the

lithium are selected for WTmetaD analysis. We employ Gaussian “hills” with a deposition rate of 100 fs, width of 0.20 Å, bias factor of 50, and height of 5.0 kJ/mol for all types of SSEs. A pair of walls is applied to limit the $Li_x \in [2.5 \text{ nm}, 4.0 \text{ nm}]$, $Li_y \in [1.5 \text{ nm}, 3.0 \text{ nm}]$ and $Li_z \in [1.5 \text{ nm}, 3.0 \text{ nm}]$ to constrain diffusion in the area with a volume of 3.375 nm³.

3. Supplementary Note 3

Free energy profiles of tilted tetrahedron.

The free energy profiles of tilted tetrahedron (F) at 300 K as functions of polar (θ) and azimuthal (ϕ) angle defined by P-S (or Si-S, Si-Cl) bonds (**Figure 5b**) in tilted tetrahedrons are obtained from unbiased NNMDs as:

$$F(\theta_i) = k_B T \ln \left(\int d\phi_i p(\theta_i, \phi_i) \right) \quad (1)$$

$$F(\phi_i) = k_B T \ln \left(\int d\theta_i p(\theta_i, \phi_i) \right) \quad (2)$$

where θ_i and ϕ_i denote polar and azimuthal angles of the i th tetrahedron, respectively, $p(\theta_i, \phi_i)$ is the distribution of the oriented tetrahedral.

4. Supplementary Note 4

Calculation of configurational disorder.

The tetrahedron distortion s_d is calculated through:

$$s_d = \frac{1}{\sum_j \sigma(r_{ij})} \sum_j \sigma(r_{ij}) \left[\frac{(x_{ij} + y_{ij} + z_{ij})^3}{r_{ij}^3} + \frac{(-x_{ij} + y_{ij} - z_{ij})^3}{r_{ij}^3} + \frac{(-x_{ij} - y_{ij} + z_{ij})^3}{r_{ij}^3} \right] \quad (6)$$

$$\sigma(r_{ij}) = \frac{1 - (r_{ij} - d_0/r_0)^n}{1 - (r_{ij} - d_0/r_0)^m} \quad (7)$$

Where r_{ij} represents the magnitude of the vector connecting atom i to atom j , and x_{ij} , y_{ij} , and z_{ij} are its' three components corresponding to the X, Y, and Z axes. $\sigma(r_{ij})$ is

a switching function applied to the distance between atoms i and j . We choose 1.2 nm for d_0 and 0.3 nm for r_0 .

5. Supplementary Note 5

Calculation of lithium conductivity.

For getting the conductivity at room temperature, we performed a wide range of NNMD simulations under 300 to 1200 K. Then we first computed the diffusion coefficient (D) using the mean square displacement (MSD) (**Supplementary Figure 42**) of lithium:

$$D = \frac{MSD(t)}{2d\Delta t} = \frac{|x_i(t) - x_i(t_0)|^2 + |y_i(t) - y_i(t_0)|^2 + |z_i(t) - z_i(t_0)|^2}{2d\Delta t} \quad (8)$$

After having D at high temperatures (≥ 900 K), we extrapolated D at room temperature 300 K. Finally, the conductivity (σ) is calculated from the Nernst-Einstein relation:

$$\sigma = \frac{Nq^2}{Vk_B T} D \quad (9)$$

Where N is the number of lithium ions, V is the total volume of the simulation cell, q is the charge of the lithium-ion, T is the temperature, and k_B is the Boltzmann constant.

Additional References

- 1 Adeli, P. *et al.* Boosting Solid-State Diffusivity and Conductivity in Lithium Superionic Argyrodites by Halide Substitution. *Angew. Chem. Int. Ed.* **58**, 8681-8686 (2019).
- 2 Hart, G. L. W., Nelson, L. J. & Forcade, R. W. Generating derivative structures at a fixed concentration. *Comput. Mater. Sci.* **59**, 101-107 (2012).
- 3 Jain, A. *et al.* A high-throughput infrastructure for density functional theory calculations. *Comput. Mater. Sci.* **50**, 2295-2310 (2011).
- 4 Barroso-Luque, L. *et al.* smol: A Python package for cluster expansions and beyond. *J. Open Source Softw.* **7**, 4504 (2022).
- 5 Kresse, G. & Furthmüller, J. Efficient iterative schemes for ab initio total-energy calculations using a plane-wave basis set. *Phys. Rev. B* **54**, 11169-11186 (1996).
- 6 Perdew, J. P., Burke, K. & Ernzerhof, M. Generalized Gradient Approximation Made Simple. *Phys. Rev. Lett.* **77**, 3865-3868 (1996).
- 7 Grimme, S., Antony, J., Ehrlich, S. & Krieg, H. A consistent and accurate ab initio parametrization of density functional dispersion correction (DFT-D) for the 94 elements H-Pu. *J. Chem. Phys.* **132**, 154104 (2010).
- 8 Invernizzi, M. & Parrinello, M. Rethinking Metadynamics: From Bias Potentials to Probability Distributions. *J. Phys. Chem. Lett.* **11**, 2731-2736 (2020).
- 9 Invernizzi, M., Piaggi, P. M. & Parrinello, M. Unified Approach to Enhanced Sampling. *Phys. Rev. X* **10** (2020).
- 10 Zhang, L. F., Han, J. Q., Wang, H., Car, R. & Weinan, E. Deep Potential Molecular Dynamics: A Scalable Model with the Accuracy of Quantum Mechanics. *Phys. Rev. Lett.* **120**, 6 (2018).
- 11 Wang, H., Zhang, L., Han, J. & E, W. DeePMD-kit: A deep learning package for many-body potential energy representation and molecular dynamics. *Comput. Phys. Commun.* **228**, 178-184 (2018).

- 12 Zhang, Y. *et al.* DP-GEN: A concurrent learning platform for the generation of reliable deep learning based potential energy models. *Comput. Phys. Commun.* **253**, 107206 (2020).
- 13 Thompson, A. P. *et al.* LAMMPS - a flexible simulation tool for particle-based materials modeling at the atomic, meso, and continuum scales. *Comput. Phys. Commun.* **271**, 108171 (2022).
- 14 Kapil, V. *et al.* i-PI 2.0: A universal force engine for advanced molecular simulations. *Comput. Phys. Commun.* **236**, 214-223 (2019).
- 15 Hoffmann, M. *et al.* Deeptime: a Python library for machine learning dynamical models from time series data. *Mach. learn.: sci. technol.* **3**, 015009 (2022).
- 16 Branduardi, D., Gervasio, F. L. & Parrinello, M. From A to B in free energy space. *J. Chem. Phys.* **126** (2007).
- 17 Díaz Leines, G. & Ensing, B. Path Finding on High-Dimensional Free Energy Landscapes. *Phys. Rev. Lett.* **109**, 020601 (2012).